

WASP-193 b: An extremely low-density super-Neptune

Khalid Barkaoui^{1,2,3,4}*, Francisco J. Pozuelos^{5,1} †, Coel Hellier⁶, Barry Smalley⁶, Louise D. Nielsen^{7,8}, Caroline Dorn⁹, Prajwal Niraula³, Michaël Gillon¹, Julien de Wit³, Ravit Helled⁹, Simon Müller⁹, Emmanuel Jehin¹⁰, Brice-Olivier Demory¹¹, V. Van Grootel¹⁰, Abderahmane Soubkiou^{2,12}, Mourad Ghachoui^{1,2}, David. R. Anderson¹³, Zouhair Benkhaldoun², Francois Bouchy⁷, Artem Burdanov³, Laetitia Delrez^{1,10}, Elsa Ducrot^{14,15}, Lionel Garcia¹, Abdelhadi Jabiri², Monika Lendl⁷, Pierre F. L. Maxted⁶, Catriona A. Murray¹⁶, Peter Pihlmann Pedersen¹⁷, Didier Queloz^{7,17}, Daniel Sebastian¹⁸, Oliver Turner^{7,19}, Stephane Udry⁷, Mathilde Timmermans¹, Amaury H. M. J. Triaud¹⁸ and Richard G. West^{13,20}

¹Astrobiology Research Unit, Université de Liège, 19C Allée du 6 Août, 4000 Liège, Belgium

²Oukaïmeden Observatory, High Energy Physics and Astrophysics Laboratory, Faculty of sciences Semlalia, Cadi Ayyad University, Marrakech, Morocco

³Department of Earth, Atmospheric and Planetary Science, Massachusetts Institute of Technology, 77 Massachusetts Avenue, Cambridge, MA 02139, USA

⁴Instituto de Astrofísica de Canarias (IAC), Calle Vía Láctea s/n, 38200, La Laguna, Tenerife, Spain

⁵Instituto de Astrofísica de Andalucía (IAA-CSIC), Glorieta de la Astronomía s/n, 18008 Granada, Spain

⁶Astrophysics Group, Keele University, Staffordshire, ST5 5BG, UK

⁷Observatoire de Genève, Université de Genève, Chemin Pegasi 51, 1290 Sauverny, Switzerland

⁸European Southern Observatory, Karl-Schwarzschildstr. 2, D-85748 Garching bei München, Germany

⁹University of Zurich, Institute of Computational Sciences, Winterthurerstrasse 190, CH-8057 Zurich, Switzerland

¹⁰Space sciences, Technologies and Astrophysics Research (STAR) Institute, Université de Liège, Belgium

¹¹Center for Space and Habitability, University of Bern, Gesellschaftsstrasse 6, CH-3012, Bern, Switzerland

¹²Instituto de Astrofísica e Ciências do Espaço, Universidade do porto, CAUP, Rua das Estrelas, 150-762 Porto, Portugal

¹³Department of Physics, University of Warwick, Gibbet Hill Road, Coventry CV4 7AL, UK

¹⁴Paris Region Fellow, Marie Skłodowska-Curie Action ¹⁵AIM, CEA, CNRS, Université Paris-Saclay, Université de Paris, F-91191 Gif-sur-Yvette, France

¹⁶Department of Astrophysical & Planetary Sciences, University of Colorado Boulder, 2000 Colorado Avenue, Boulder, CO 80309, USA

¹⁷Cavendish Laboratory, JJ Thomson Avenue, Cambridge, CB3 0H3, UK

¹⁸School of Physics & Astronomy, University of Birmingham, Edgbaston, Birmingham, B15 2TT, UK

¹⁹Space Forge, Unit 10, Eastgate Business Park, Wentloog Ave, Rumney, Cardiff, CF3 2EY

²⁰Centre for Exoplanets and Habitability, University of Warwick, Gibbet Hill Road, Coventry CV4 7AL, UK

Gas giants transiting bright nearby stars are stepping stones for our understanding of planetary system formation and evolution mechanisms. This paper presents a particularly interesting new specimen of this kind of exoplanet discovered by the WASP-South transit survey,

*corresponding author (khalid.barkaoui@uliege.be)

†corresponding author (pozuelos@iaa.es)

WASP-193 b. This planet completes an orbit around its $V_{\text{mag}} = 12.2$ F9 main-sequence host star every 6.25 d. Our analyses found that WASP-193 b has a mass of $M_p = 0.139 \pm 0.029 M_{\text{Jup}}$ and a radius of $R_p = 1.464 \pm 0.058 R_{\text{Jup}}$, translating into an extremely low density of $\rho_p = 0.059 \pm 0.014 \text{ g cm}^{-3}$. The planet was confirmed photometrically by the 0.6-m TRAPPIST-South, the 1.0-m SPECULOOS-South telescopes, and the TESS mission, and spectroscopically by the ESO-3.6-m/HARPS and Euler-1.2-m/CORALIE spectrographs. The combination of its large transit depth ($dF \sim 1.4 \%$), its extremely-low density, its high-equilibrium temperature ($T_{\text{eq}} = 1254 \pm 31 \text{ K}$), and the infrared brightness of its host star (magnitude $K_{\text{mag}} = 10.7$) makes WASP-193 b an exquisite target for characterization by transmission spectroscopy (transmission spectroscopy metric: $TSM^1 \sim 600$). One single JWST transit observation would yield detailed insights into its atmospheric properties and planetary mass², within ~ 0.1 dex and $\sim 1\%$ (vs $\sim 20\%$ currently with radial velocity data) respectively.

WASP-193 was observed by the WASP-South³ survey in 2006–2008 and 2011–2012. The WASP photometry revealed a periodic signal consistent with transits of a giant planet with an orbital period of 6.25d (see Methods). Ground-based photometric follow-up was obtained using the TRAPPIST-South^{4,5} and SPECULOOS-South^{6–8} telescopes, and spectroscopic measurements were performed using CORALIE⁹ and HARPS¹⁰ spectrographs.

We used TRAPPIST-South and SPECULOOS-South to observe five transits of WASP-193 b, one in the $I + z$ filter (02 January 2015), one in a ‘Blue-Blocking’ (BB) filter (06 April 2015), one in the Sloan- z' filter (27 January 2017), and two in the Johnson- B filter (08 June 2019). Additional photometric measurements were collected by the *TESS*¹¹ mission with 1800, 600, and 120 s cadences, of which we used in our analysis the PCDSAP fluxes corresponding to 600 and 120 s (see Methods). All these photometric observations are summarized in Table 4 and are presented in Figure 1 (left panel).

In addition, we used the Euler-1.2m/CORALIE and ESO-3.6m/HARPS spectrographs to observe WASP-193. We obtained 12 and 11 spectroscopic measurements with CORALIE and HARPS in 2015 and 2019, respectively. We used the cross-correlation technique¹² to extract the radial velocity measurements (see Methods). The resulting radial velocity curve is presented in Figure 1 (right panel).

All the follow-up data were consistent with the planetary origin of the transit signal identified by WASP. The high-precision follow-up light curves acquired in different filters showed no chromatic dependence. Indeed, the transit depths obtained with different bands agree at 1σ level (see Table 2). The radial velocities phased up with the transit time and period of 6.25 d, consistent with the transit timings, and the bisector analysis of the HARPS and CORALIE spectra¹³ did not reveal any dependence of the measured radial velocities with the bisector span (see Figure 1, right panels).

To constrain the stellar atmospheric parameters of WASP-193, we co-added HARPS and CORALIE spectra to produce a single stellar spectrum with a high signal-to-noise ratio ($S/N \sim 75$) and ana-

lyzed it as described in ref.¹⁴. This analysis enabled us to constrain the following parameters: the spectral type, the metallicity $[Fe/H]$, the effective temperature T_{eff} , the surface gravity $\log g_*$, and the rotational velocity $V \sin(i)$ (see Methods). The resulting values show that WASP-193 is a F9-type Sun-like star with $T_{\text{eff}} = 6076 \pm 120$ K, $\log g_* = 4.1 \pm 0.1$ dex, $[Fe/H] = -0.06 \pm 0.09$ dex and $V \sin(i) = 4.3 \pm 0.8$ km s⁻¹. Using our measured T_{eff} , the star’s magnitudes in different broadband filters (see Table 1), and its Gaia eDR3 parallax¹⁵, we conducted a SED-fitting to derive a stellar radius of $R_* = 1.225^{+0.032}_{-0.029} R_{\odot}$ by employing the *EXOFASTv2*¹⁶ pipeline. Adopting T_{eff} , $[Fe/H]$, and R_* as the basic input set, we then derived the stellar mass M_* and age t_* from stellar evolutionary modeling. We used the CLES (Code Liégeois d’Évolution Stellaire¹⁷), building the best-fit stellar evolutionary track according to the input parameters following the Levenberg-Marquadt minimisation scheme, as explained in ref.¹⁸. We obtained $M_* = 1.102 \pm 0.070 M_{\odot}$ and $t_* = 4.43 \pm 1.92$ Gyr. Table 1 summarizes the stellar parameters inferred from our analyses.

We derived the system’s parameters by conducting a global model fitting together the photometric and spectroscopic data using the latest version of the Markov Chain Monte Carlo (MCMC) code described in ref.¹⁹, employing the Mandel & Agol²⁰ and a 2-body Keplerian models²¹, respectively (see Methods). Table 2 shows the deduced stellar and planetary physical parameters along with their 1σ intervals.

We find that planet has a radius of $R_p = 1.464 \pm 0.058 R_{\text{Jup}}$ and a mass of $M_p = 0.139 \pm 0.029 M_{\text{Jup}}$ ($\sim 3 M_{\text{Neptune}}$), resulting in a surprisingly low density of $\rho_p = 0.059 \pm 0.014$ g/cm³ (see top panel in Figure 2). This extremely low density positioned WASP-193 b as the second lightest planet discovered so far after Kepler 51 d ($\rho = 0.04 \pm 0.01$ g/cm³) (both planets’ densities connected at 1σ level), and as the lightest planet over the hot-Jupiter population. It is worth noting that we restricted our comparison to planets that are precisely characterized, with dynamical masses and radii precisions better than 25% and 8%, respectively²². This approach aimed to eliminate any potential bias introduced by comparing WASP-193 b with inadequately characterized planets that could impede conclusive findings. Notably, these poorly characterized planets exhibit a 1σ level association with distinct planet populations, further emphasizing the challenge of performing a meaningful analysis of their nature due to significant degeneracies.

Remarkably, considering the irradiation of about $S_p = 6 \times 10^5$ W/m² (or 440× larger than that of Earth) inferred from our analysis (see the bottom panel in Figure 2), classical evolution models of irradiated giant planets^{23–26} are not able to reproduce WASP-193 b’s radius. Indeed, using the irradiated gas giant model from ref.²³ for a core mass of 0 to 10 M_{\oplus} and age between 1.0 to 4.5 Gyrs, the predicted radius is found to be 0.9–1.1 R_{Jup} . We also used the equation derived by ref.²⁵ from 35 exoplanets with $M_p < 150 M_{\oplus}$. In this case, the resulting predicted radius is found to be $R_p = 0.82 \pm 0.14 R_{\text{Jup}}$. Finally, we used the model of ref.²⁶ to calculate the radius of the planet using data from 286 hot Jupiters with known masses and radii. In this scenario, the predicted radius measures $R_p = 1.1 \pm 0.1 R_{\text{Jup}}$. Therefore, WASP-193 b joins thus the sub-group of ‘anomalously large’ irradiated gas giants²⁷.

Planet Interior

In the core accretion model, planets at this mass range are expected to have non-negligible amounts of heavy elements²⁸. This is at odds with the low density of WASP-193 b. Alternatively, the planet could have formed by disk instability, as it was recently shown by ref.²⁹ that magnetically controlled disk fragmentation could lead to intermediate-mass clumps of H-He. The formation mechanism of planets like WASP-193 b remains uncertain, including its potential orbital evolution and we hope that future formation models can address its formation mechanism.

We calculated the evolution of WASP-193 b following the framework presented by ref.³⁰, which assumes a *hot start* core accretion formation scenario³¹. The models use the equations of state³² for H-He and for a 50-50 water-rock mix³³. The planetary radius corresponds to the photosphere where the optical depth drops below 2/3. Gas opacities are taken from ref.³⁴. Additional details on the interior evolution model can be found in ref.³⁰. We adapted the evolution models of ref.³⁰ to account for the evolution of the host star where the stellar luminosity follows a pre-calculated stellar evolution track. The luminosity as a function of time was calculated with the MESA Isochrones and Stellar Tracks (MIST)^{35,36} with the mass of $M_\star = 1.068 M_\odot$ and slightly sub-solar metallicity $[Fe/H] = -0.06$ obtained from our spectroscopic analysis. The age-range of the planet was defined by the ages at which the stellar luminosity from the evolution tracks matched the inferred one $L = 1.87_{-0.16}^{+0.18} L_\odot$ (see also Table 1). As there is no clear correlation between stellar metallicity and the composition of giant planets³⁷, the bulk composition of WASP-193 b cannot be inferred from the measured stellar $[Fe/H]$. As a result, we considered two end members of the planetary composition (i.e., planetary metallicity). First, we calculated the evolution of WASP-193 b with $Z = 0.0$, representing the lowest metallicity case. Naively, one would expect a pure H-He planet to yield the largest radius (and lowest density) at a given time. However, since a metal-enriched atmosphere has a higher opacity and therefore delays the cooling, a planet with $Z > 0$ could actually contract more slowly³⁸. It has been shown that a turn-over value of Z exists for which the effect of the increased density wins over the delayed cooling. After that, the planetary size decreases with increasing Z (see ref.³⁸ for further details). For planet WASP-193 b, the turn-over value is $Z = 0.1$. Therefore, we also considered the evolution of WASP-193 b with $Z = 0.1$. The evolution of the planetary radius for the two cases is shown in Figure 3. While the enriched atmosphere in the $Z = 0.1$ case yielded a larger radius until around 1 Gyr, it is clear that neither model can reproduce the observed radius of WASP-193 b for the possible stellar ages. The influence of the stellar evolution is more profound at early times when the star has a higher luminosity. The planet cools down as the stellar luminosity decreases and the star reaches the main sequence. We find that the planet has a size comparable to that of WASP-193 b only for an age of a few 10 Myr, which is inconsistent with the estimated age of the host star. Clearly, the large observed radius of $\sim 1.5 R_{\text{Jup}}$ at an age of several Gyr cannot be reproduced unless other mechanisms are at work, these include processes that (1) delay the cooling of the planet, or (2) deposit heat deep in the planetary interior and mass loss, all of which are in principle dependent on metallicity Z . We discuss such mechanisms below.

Delay in planetary cooling Inefficient cooling can be caused by various processes, such as an enhanced atmospheric opacity that leads to longer cooling time scales, interiors that are not fully convective, and phase separations. For the former, as we show in Figure 3, the effect of prolonged cooling via opacity enhancement is insufficient to explain WASP-193 b’s large radius. Additionally, it would be possible that the opacity is enhanced due to dust grains or cloud decks, which were not included in our models. However, it is unlikely that this would increase the radius beyond a few percent^{39,40}. Also, in the case of a not fully convective interior, the planet contracts at a lower rate. This can occur when the interior consists of boundary layers and/or composition gradients^{41–43}. Such a configuration can lead to much higher internal temperatures at a given age⁴⁴ and is expected to lead to an increase in radius by up to $\sim 10\%$ ⁴⁵. Therefore, this scenario also cannot explain the large observed radius. Phase separation could also lead to slower cooling. In giant planets, He-rain can delay the planetary cooling⁴⁶. Its ability to increase the planetary radii is, however, limited to a few percent⁴⁷. More importantly, a planet of $\sim 0.14 M_{\text{Jup}}$ as WASP-193 b is not expected to reach internal pressures that are high enough for He to become immiscible⁴⁷. A self-consistent model that incorporates layered-convection, tidal heating, boundary layers as well as enhanced opacities and dust-rich atmospheres to delay the cooling to its maximum would be required to fully evaluate whether the combined mechanisms are sufficient to explain the measured radius. However, the observed radius of WASP-193 b is 40-50% larger than predictions from evolution models. Therefore, these mechanisms are unlikely to add up to account for the inflated radius fully.

Heat deposition and mass loss The planet may be heated at depth due to Ohmic dissipation or tidal heating. However, tidal heating is unlikely to be the mechanism that inflates hot Jupiters since it has been observed that the inflated radii correlate with stellar flux better than with the distance to the hot star^{25,48}. Currently, Ohmic dissipation seems to be the most promising mechanism⁴⁹. This is because the atmosphere of WASP-193 b is sufficiently hot ($T_{\text{eq}} \sim 1250 \text{ K}$) that trace elements in the H-He gas can be partially ionized and allow for atmospheric currents to penetrate deep into the interior. For hot Jupiters, the radius inflation power depends on the incident flux⁵⁰. If WASP-193 b experiences similar inflation mechanisms, this suggests that mechanisms that are coupled to stellar heating, including Ohmic dissipation, are favorable, and possibly, multiple mechanisms are at play. Additional heating in the deep interior could be occurring together with semi-convective and/or boundary layers. This could effectively trap some of the deposited energy and delay the planetary cooling.

We estimate the additional energy required to explain the observed radius of WASP-193 b independent of the heating mechanism. We determine the planetary total internal energy E_0 at a time t_0 where the planet’s radius matches the observed one. The energy required for the additional inflation is then $\Delta E = E_0 - E_{\text{today}}$, where E_{today} is the internal energy at the mean stellar age. We find that $t_0 = 40 \text{ Myr}$ ($Z = 0$) and 60 Myr ($Z = 0.1$), which yielded a similar $\Delta E \sim 10^{40} \text{ erg}$ for the two cases. For comparison, the energy WASP-193 b receives today by the stellar irradiation is $\sim 5 \times 10^{36} \text{ erg/yr}$, about four orders of magnitude lower.

Finally, the relatively low mass of WASP-193 b, its high stellar irradiation, and its location at the edge of the sub-Jovian valley in the M-R diagram might hint that it may be losing mass. If this is the case, the extended observed radius may be related to material evaporating and leaving the planet. However, this is only a speculation, and we stress that there is no indication in the measurements for atmospheric loss. It is possible to use theoretical models of mass loss for highly irradiated planets to estimate whether atmospheric escape is significant for WASP-193 b. We calculate the restricted Jeans escape parameter $\Lambda \propto M_p/T_{eq}R_p$ from ref.⁵¹, which can be used to identify planets for which atmospheric escape is important. For WASP-193 b we find $\Lambda = 3.7$. It was shown in ref.⁵¹ that Λ values lower than the critical value of $\Lambda_T = 15 - 35$ correspond to significant atmospheric loss. As a result, the atmospheric mass loss could be important for WASP-193 b. However, we emphasize that detailed hydrodynamic simulations should be performed to fully assess the importance of atmospheric escape for WASP-193 b.

Overall, the evolution model cannot explain the observations of WASP-193 b, despite its being state-of-the-art. A self-consistent model that incorporates layered convection, boundary layers, as well as enhanced opacities, and dust-rich atmospheres to delay the cooling to its maximum would be required to evaluate whether the combined mechanisms are sufficient to explain the measured radius. However, this would require considerable effort in improving existing evolution models, which is out of the scope of this study. Besides advances in modelling, additional constraints on the atmospheric escape, composition, and temperature structure might be obtained by conducting transit spectroscopy using the JWST, providing key information to unravel the nature of this low-density planet, as discussed in the following.

Atmospheric characterization prospects Owing to its remarkably low density, the hot Jupiter WASP-193 b is a prime target for atmospheric characterization. As highlighted in Figure 4, its transmission spectroscopy metric (TSM^1) is amongst the highest to date (~ 600). We used the TIERRA retrieval framework⁵² to assess quantitatively the insights that would be accessible with a single visit of JWST. To this end, we performed an injection-retrieval on a synthetic WASP-193 b atmosphere using abundances consistent with WASP-39 b (see Methods). We assume the use of NIRSpec/Prism as its wavelength coverage provides the best trade-off for atmospheric exploration. Figure 5 presents the synthetic data, the best fit, and the retrieved planetary parameters. We find that a single transit observation can yield the abundances of strong absorbers within 0.1 dex, assuming no significant opacity challenge⁵² as expected for hot Jupiters⁵³. Most importantly, we find that the planetary mass is tightly constrained within $\sim 1\%$ in comparison to the current $\sim 20\%$ precision achieved with radial velocity measurements. This tight constraint is enabled by the independent constraints on the atmospheric scale height ($H = 3008 \pm 119$ km), temperature, and abundance accessible via transmission spectroscopy at such high TSM^2 . While a single visit with JWST/NIRSpec/Prism would provide the most insights into the planetary atmosphere, a single JWST/NIRISS SOSS observation would also allow to detect the He absorption triplet, this would provide preliminary insights into the current atmospheric loss^{54,55}. Ground-based high-resolution

measures could later complement this picture by constraining the line profile⁵⁶, helping to validate or dismiss the hypothesis that atmospheric loss is responsible for the observed low-density nature of this planet. Moreover, using the NIRISS/SOSS, it would also be possible to place some constraints on the atmospheric metallicity (M/H), carbon-to-oxygen ratio (C/O), and potassium-to-oxygen ratio (K/O)⁵⁷, shedding some light into the formation process of WASP-193 b. For example, the hypothetical combination of a super-solar metallicity, super-solar K/O ratio, and sub-solar C/O ratio may suggest that the planet formed beyond the H₂O snow line followed by inward migration, producing an efficient accretion of planetesimals⁵⁸⁻⁶⁰. Therefore, in general terms, the characteristics of WASP-193 b, along with its exquisite suitability for atmospheric characterization, position it as a benchmark planet for gaining insights into the properties of the population of low-density planets.

References

1. Kempton, E. M. R. *et al.* A Framework for Prioritizing the TESS Planetary Candidates Most Amenable to Atmospheric Characterization. *Publications of the Astronomical Society of the Pacific* **130**, 114401 (2018). [1805.03671](#).
2. de Wit, J. & Seager, S. Constraining Exoplanet Mass from Transmission Spectroscopy. *Science* **342**, 1473–1477 (2013). [1401.6181](#).
3. Pollacco, D. L. *et al.* The WASP project and the SuperWASP cameras. *Publications of the Astronomical Society of the Pacific* **118**, 1407–1418 (2006). URL <https://doi.org/10.1086/508556>.
4. Gillon, M. *et al.* TRAPPIST: a robotic telescope dedicated to the study of planetary systems. *EPJ Web of Conferences* **11**, 06002 (2011). URL <https://doi.org/10.1051/epjconf/20101106002>.
5. Jehin, E. *et al.* TRAPPIST: TRAnsiting Planets and Planetesimals Small Telescope. *The Messenger* **145**, 2–6 (2011).
6. Burdanov, A., Delrez, L., Gillon, M. & Jehin, E. SPECULOOS exoplanet search and its prototype on TRAPPIST. *ArXiv e-prints* (2017). [1710.03775](#).
7. Delrez, L. *et al.* SPECULOOS: a network of robotic telescopes to hunt for terrestrial planets around the nearest ultracool dwarfs. *ArXiv e-prints* (2018). [1806.11205](#).
8. Jehin, E. *et al.* The SPECULOOS Southern Observatory Begins its Hunt for Rocky Planets. *The Messenger* **174**, 2–7 (2018).
9. Queloz, D. *et al.* Extrasolar Planets in the Southern Hemisphere: The CORALIE Survey. In Bergeron, J. & Renzini, A. (eds.) *From Extrasolar Planets to Cosmology: The VLT Opening Symposium*, 548 (2000).
10. Mayor, M. *et al.* Setting New Standards with HARPS. *The Messenger* **114**, 20–24 (2003).
11. Ricker, G. R. *et al.* Transiting Exoplanet Survey Satellite (TESS). *Journal of Astronomical Telescopes, Instruments, and Systems* **1**, 014003 (2015).
12. Baranne, A. *et al.* ELODIE: A spectrograph for accurate radial velocity measurements. *Astron. Astrophys., Suppl. Ser.* **119**, 373–390 (1996).
13. Torres, G., Konacki, M., Sasselov, D. D. & Jha, S. Testing blend scenarios for extrasolar transiting planet candidates. i. OGLE-TR-33: A false positive. *The Astrophysical Journal* **614**, 979–989 (2004). URL <https://doi.org/10.1086/423734>.
14. Doyle, A. P. *et al.* Accurate spectroscopic parameters of WASP planet host stars. *Mon. Not. R. Astron. Soc.* **428**, 3164–3172 (2013). [1210.5931](#).

15. Gaia Collaboration. VizieR Online Data Catalog: Gaia EDR3 (Gaia Collaboration, 2020). *VizieR Online Data Catalog I/350* (2020).
16. Eastman, J. D. *et al.* EXOFASTv2: A public, generalized, publication-quality exoplanet modeling code. *arXiv e-prints* arXiv:1907.09480 (2019). [1907.09480](https://arxiv.org/abs/1907.09480).
17. Scufflaire, R. *et al.* CLÉS, Code Liégeois d'Évolution Stellaire. *Astrophysics and Space Science* **316**, 83–91 (2008). [0712.3471](https://doi.org/10.1007/s11231-008-9111-1).
18. Salmon, S. J. A. J., Van Grootel, V., Buldgen, G., Dupret, M. A. & Eggenberger, P. Reinvestigating α Centauri AB in light of asteroseismic forward and inverse methods. *Astron. Astrophys.* **646**, A7 (2021). [2011.14932](https://arxiv.org/abs/2011.14932).
19. Gillon, M. *et al.* The TRAPPIST survey of southern transiting planets. I. Thirty eclipses of the ultra-short period planet WASP-43 b. *Astron. Astrophys.* **542**, A4 (2012). [1201.2789](https://arxiv.org/abs/1201.2789).
20. Mandel, K. & Agol, E. Analytic Light Curves for Planetary Transit Searches. *Astrophys. J., Letters* **580**, L171–L175 (2002). [astro-ph/0210099](https://arxiv.org/abs/astro-ph/0210099).
21. Murray, C. D. & Correia, A. C. M. *Keplerian Orbits and Dynamics of Exoplanets*, 15–23 (2010).
22. Luque, R. & Pallé, E. Density, not radius, separates rocky and water-rich small planets orbiting M dwarf stars. *Science* **377**, 1211–1214 (2022). [2209.03871](https://arxiv.org/abs/2209.03871).
23. Fortney, J. J., Marley, M. S. & Barnes, J. W. Planetary Radii across Five Orders of Magnitude in Mass and Stellar Insolation: Application to Transits. *Astrophys. J.* **659**, 1661–1672 (2007). [astro-ph/0612671](https://arxiv.org/abs/astro-ph/0612671).
24. Baraffe, I., Chabrier, G. & Barman, T. Structure and evolution of super-Earth to super-Jupiter exoplanets. I. Heavy element enrichment in the interior. *Astron. Astrophys.* **482**, 315–332 (2008). [0802.1810](https://arxiv.org/abs/0802.1810).
25. Weiss, L. M. *et al.* The Mass of KOI-94d and a Relation for Planet Radius, Mass, and Incident Flux. *Astrophys. J.* **768**, 14 (2013). [1303.2150](https://arxiv.org/abs/1303.2150).
26. Sestovic, M., Demory, B.-O. & Queloz, D. Investigating hot-Jupiter inflated radii with hierarchical Bayesian modelling. *Astronomy & Astrophysics* **616**, A76 (2018). [1804.03075](https://arxiv.org/abs/1804.03075).
27. Lopez, E. D. & Fortney, J. J. RE-INFLATED WARM JUPITERS AROUND RED GIANTS. *The Astrophysical Journal* **818**, 4 (2016). URL <https://doi.org/10.3847/0004-637x/818/1/4>.
28. Helled, R. *et al.* Giant Planet Formation, Evolution, and Internal Structure. In Beuther, H., Klessen, R. S., Dullemond, C. P. & Henning, T. (eds.) *Protostars and Planets VI*, 643 (2014). [1311.1142](https://arxiv.org/abs/1311.1142).

29. Deng, H., Mayer, L. & Helled, R. Formation of intermediate-mass planets via magnetically controlled disk fragmentation. *Nature Astronomy* **5**, 440–444 (2021).
30. Müller, S. & Helled, R. Synthetic evolution tracks of giant planets. *Monthly Notices of the Royal Astronomical Society* **507**, 2094–2102 (2021).
31. Marley, M. S., Fortney, J. J., Hubickyj, O., Bodenheimer, P. & Lissauer, J. J. On the Luminosity of Young Jupiters. *Astrophys. J.* **655**, 541–549 (2007). [astro-ph/0609739](#).
32. Chabrier, G., Mazevet, S. & Soubiran, F. A new equation of state for dense hydrogen–helium mixtures. *The Astrophysical Journal* **872**, 51 (2019).
33. More, R., Warren, K., Young, D. & Zimmerman, G. A new quotidian equation of state (qeos) for hot dense matter. *The Physics of fluids* **31**, 3059–3078 (1988).
34. Freedman, R. S. *et al.* Gaseous mean opacities for giant planet and ultracool dwarf atmospheres over a range of metallicities and temperatures. *The Astrophysical Journal Supplement Series* **214**, 25 (2014).
35. Choi, J. *et al.* Mesa Isochrones and Stellar Tracks (MIST). I. Solar-scaled Models. *Astrophys. J.* **823**, 102 (2016). [1604.08592](#).
36. Dotter, A. MESA Isochrones and Stellar Tracks (MIST) 0: Methods for the Construction of Stellar Isochrones. *Astrophys. J., Suppl. Ser.* **222**, 8 (2016). [1601.05144](#).
37. Teske, J. K., Thorngren, D., Fortney, J. J., Hinkel, N. & Brewer, J. M. Do Metal-rich Stars Make Metal-rich Planets? New Insights on Giant Planet Formation from Host Star Abundances. *Astron. J.* **158**, 239 (2019). [1912.00255](#).
38. Müller, S., Helled, R. & Cumming, A. The challenge of forming a fuzzy core in jupiter. *Astronomy & Astrophysics* **638**, A121 (2020).
39. Vazan, A., Kovetz, A., Podolak, M. & Helled, R. The effect of composition on the evolution of giant and intermediate-mass planets. *Mon. Not. R. Astron. Soc.* **434**, 3283–3292 (2013). [1307.2033](#).
40. Poser, A. J., Nettelmann, N. & Redmer, R. The Effect of Clouds as an Additional Opacity Source on the Inferred Metallicity of Giant Exoplanets. *Atmosphere* **10**, 664 (2019). [1911.01191](#).
41. Chabrier, G. & Baraffe, I. Heat transport in giant (exo) planets: a new perspective. *The Astrophysical Journal Letters* **661**, L81 (2007).
42. Helled, R. & Stevenson, D. The fuzziness of giant planets’ cores. *The Astrophysical Journal Letters* **840**, L4 (2017).
43. Vazan, A., Helled, R. & Guillot, T. Jupiter’s evolution with primordial composition gradients. *Astronomy & Astrophysics* **610**, L14 (2018).

44. Leconte, J. & Chabrier, G. A new vision of giant planet interiors: Impact of double diffusive convection. *Astronomy & Astrophysics* **540**, A20 (2012).
45. Kurokawa, H. & Inutsuka, S.-i. On the radius anomaly of hot jupiters: Reexamination of the possibility and impact of layered convection. *The Astrophysical Journal* **815**, 78 (2015).
46. Stevenson, D. & Salpeter, E. The dynamics and helium distribution in hydrogen-helium fluid planets. *Astrophysical Journal Supplement Series* **35**, 239–261 (1977).
47. Fortney, J. J. & Hubbard, W. Effects of helium phase separation on the evolution of extrasolar giant planets. *The Astrophysical Journal* **608**, 1039 (2004).
48. Laughlin, G., Crismani, M. & Adams, F. C. On the Anomalous Radii of the Transiting Extrasolar Planets. *Astrophys. J., Letters* **729**, L7 (2011). [1101.5827](#).
49. Fortney, J. J., Dawson, R. I. & Komacek, T. D. Hot jupiters: Origins, structure, atmospheres. *Journal of Geophysical Research: Planets* **126**, e2020JE006629 (2021).
50. Thorngren, D. P. & Fortney, J. J. Bayesian Analysis of Hot-Jupiter Radius Anomalies: Evidence for Ohmic Dissipation? *Astron. J.* **155**, 214 (2018). [1709.04539](#).
51. Fossati, L. *et al.* Aeronomical constraints to the minimum mass and maximum radius of hot low-mass planets. *Astron. Astrophys.* **598**, A90 (2017). [1612.05624](#).
52. Niraula, P. *et al.* The impending opacity challenge in exoplanet atmospheric characterization. *Nature Astronomy* **6**, 1287–1295 (2022). [2209.07464](#).
53. Niraula, P., de Wit, J., Gordon, I. E., Hargreaves, R. J. & Sousa-Silva, C. Origin and extent of the opacity challenge for atmospheric retrievals of WASP-39 b. *arXiv e-prints* arXiv:2303.03383 (2023). [2303.03383](#).
54. Seager, S. & Sasselov, D. D. Theoretical Transmission Spectra during Extrasolar Giant Planet Transits. *Astrophys. J.* **537**, 916–921 (2000). [astro-ph/9912241](#).
55. Spake, J. J. *et al.* Helium in the eroding atmosphere of an exoplanet. *Nature* **557**, 68–70 (2018). [1805.01298](#).
56. Allart, R. *et al.* Spectrally resolved helium absorption from the extended atmosphere of a warm Neptune-mass exoplanet. *Science* **362**, 1384–1387 (2018). [1812.02189](#).
57. Feinstein, A. D. *et al.* Early Release Science of the exoplanet WASP-39b with JWST NIRISS. *Nature* **614**, 670–675 (2023). [2211.10493](#).
58. Mordasini, C., van Boekel, R., Mollière, P., Henning, T. & Benneke, B. The Imprint of Exoplanet Formation History on Observable Present-day Spectra of Hot Jupiters. *Astrophys. J.* **832**, 41 (2016). [1609.03019](#).

59. Shibata, S., Helled, R. & Ikoma, M. The origin of the high metallicity of close-in giant exoplanets. Combined effects of resonant and aerodynamic shepherding. *Astron. Astrophys.* **633**, A33 (2020). [1911.02292](#).
60. Hands, T. O. & Helled, R. Super stellar abundances of alkali metals suggest significant migration for hot Jupiters. *Mon. Not. R. Astron. Soc.* **509**, 894–902 (2022). [2110.06230](#).
61. Hunter, J. D. Matplotlib: A 2d graphics environment. *Computing in Science & Engineering* **9**, 90–95 (2007).
62. van der Walt, S., Colbert, S. C. & Varoquaux, G. The NumPy Array: A Structure for Efficient Numerical Computation. *Computing in Science and Engineering* **13**, 22–30 (2011). [1102.1523](#).
63. Astropy Collaboration *et al.* Astropy: A community Python package for astronomy. *Astron. Astrophys.* **558**, A33 (2013). [1307.6212](#).
64. Jones, E., Oliphant, T. & Peterson, P. SciPy: open source scientific tools for Python (2001). URL <http://www.scipy.org>.
65. Lightkurve Collaboration *et al.* Lightkurve: Kepler and TESS time series analysis in Python. Astrophysics Source Code Library (2018). [1812.013](#).
66. Garcia, L. J. *et al.* prose: A Python framework for modular astronomical images processing. *Mon. Not. R. Astron. Soc.* (2021). [2111.02814](#).
67. Hippke, M., David, T. J., Mulders, G. D. & Heller, R. Wötan: Comprehensive Time-series Detrending in Python. *Astron. J.* **158**, 143 (2019). [1906.00966](#).
68. Bradley, L. *et al.* astropy/photutils: 1.0.0 (2020). URL <https://doi.org/10.5281/zenodo.4044744>.
69. Mollière, P. *et al.* petitRADTRANS. A Python radiative transfer package for exoplanet characterization and retrieval. *Astron. Astrophys.* **627**, A67 (2019). [1904.11504](#).
70. Maxted, P. F. L., Serenelli, A. M. & Southworth, J. Bayesian mass and age estimates for transiting exoplanet host stars. *Astron. Astrophys.* **575**, A36 (2015). [1412.7891](#).
71. Maxted, P. F. L. *et al.* Five transiting hot Jupiters discovered using WASP-South, Euler, and TRAPPIST: WASP-119 b, WASP-124 b, WASP-126 b, WASP-129 b, and WASP-133 b. *Astron. Astrophys.* **591**, A55 (2016). [1602.01740](#).
72. Baştürk, Ö., Dall, T. H., Collet, R., Lo Curto, G. & Selam, S. O. Bisectors of the HARPS cross-correlation function. The dependence on stellar atmospheric parameters. *Astron. Astrophys.* **535**, A17 (2011). [1110.0975](#).

73. Martínez Fiorenzano, A. F., Gratton, R. G., Desidera, S., Cosentino, R. & Endl, M. Line bisectors and radial velocity jitter from SARG spectra. *Astron. Astrophys.* **442**, 775–784 (2005). [astro-ph/0508096](https://arxiv.org/abs/astro-ph/0508096).
74. Jontof-Hutter, D., Dalba, P. A. & Livingston, J. H. TESS Observations of Kepler Systems with Transit Timing Variations. *Astron. J.* **164**, 42 (2022). [2207.08917](https://arxiv.org/abs/2207.08917).
75. Anderson, D. R. *et al.* Thermal emission at 4.5 and 8 μm of WASP-17b, an extremely large planet in a slightly eccentric orbit. *Mon. Not. R. Astron. Soc.* **416**, 2108–2122 (2011). [1101.5620](https://arxiv.org/abs/1101.5620).
76. Lam, K. W. F. *et al.* From dense hot Jupiter to low-density Neptune: The discovery of WASP-127b, WASP-136b, and WASP-138b. *Astron. Astrophys.* **599**, A3 (2017). [1607.07859](https://arxiv.org/abs/1607.07859).
77. Hartman, J. D. *et al.* HAT-P-65b and HAT-P-66b: Two Transiting Inflated Hot Jupiters and Observational Evidence for the Reinflation of Close-in Giant Planets. *Astron. J.* **152**, 182 (2016). [1609.02767](https://arxiv.org/abs/1609.02767).
78. Demory, B.-O. & Seager, S. Lack of Inflated radii for Kepler giant planet candidates receiving modest stellar irradiation. *The Astrophysical Journal Supplement Series* **197**, 12 (2011). URL <https://doi.org/10.1088%2F0067-0049%2F197%2F1%2F12>.
79. Stassun, K. G. *et al.* The TESS Input Catalog and Candidate Target List. *Astron. J.* **156**, 102 (2018). [1706.00495](https://arxiv.org/abs/1706.00495).
80. Cutri, R. M. *et al.* *2MASS All Sky Catalog of point sources*. (2003).
81. Henden, A. A. *et al.* VizieR Online Data Catalog: AAVSO Photometric All Sky Survey (APASS) DR9 (Henden+, 2016). *VizieR Online Data Catalog II/336* (2016).
82. Wright, E. L. *et al.* The Wide-field Infrared Survey Explorer (WISE): Mission Description and Initial On-orbit Performance. *Astron. J.* **140**, 1868–1881 (2010). [1008.0031](https://arxiv.org/abs/1008.0031).
83. Meylan, G., Madrid, J. P. & Macchetto, D. Hubble Space Telescope Science Metrics. *Publ. Astron. Soc. Pacific* **116**, 790–796 (2004). [astro-ph/0406655](https://arxiv.org/abs/astro-ph/0406655).
84. Pepe, F. A. *et al.* ESPRESSO: the Echelle spectrograph for rocky exoplanets and stable spectroscopic observations. In McLean, I. S., Ramsay, S. K. & Takami, H. (eds.) *Ground-based and Airborne Instrumentation for Astronomy III*, vol. 7735, 209 – 217. International Society for Optics and Photonics (SPIE, 2010). URL <https://doi.org/10.1117/12.857122>.
85. Dressler, A. *et al.* IMACS: The inamori-magellan areal camera and spectrograph on magellan-baade. *Publications of the Astronomical Society of the Pacific* **123**, 288–332 (2011). URL <https://doi.org/10.1086/658908>.

86. Gardner, J. P. *et al.* The James Webb Space Telescope. *Space Science Reviews* **123**, 485–606 (2006). [astro-ph/0606175](https://arxiv.org/abs/astro-ph/0606175).
87. Sing, D. K. *et al.* A continuum from clear to cloudy hot-Jupiter exoplanets without primordial water depletion. *Nature* **529**, 59–62 (2016). [1512.04341](https://doi.org/10.1038/52904341).
88. Wakeford, H. R. *et al.* HST PanCET program: A cloudy atmosphere for the promising JWST target WASP-101b. *The Astrophysical Journal* **835**, L12 (2017). URL <https://doi.org/10.3847/2041-8213/835/1/L12>.
89. Sing, D. K. *et al.* The hubble space telescope PanCET program: Exospheric mg ii and fe ii in the near-ultraviolet transmission spectrum of WASP-121b using jitter decorrelation. *The Astronomical Journal* **158**, 91 (2019). URL <https://doi.org/10.3847/1538-3881/ab2986>.
90. Skaf, N. *et al.* ARES. II. characterizing the hot jupiters WASP-127 b, WASP-79 b, and WASP-62b with the hubble space telescope. *The Astronomical Journal* **160**, 109 (2020). URL <https://doi.org/10.3847/1538-3881/ab94a3>.
91. Collier Cameron, A. *et al.* A fast hybrid algorithm for exoplanetary transit searches. *Mon. Not. R. Astron. Soc.* **373**, 799–810 (2006). [astro-ph/0609418](https://arxiv.org/abs/astro-ph/0609418).
92. Street, R. A. *et al.* Status of SuperWASP I (La Palma). *Astronomische Nachrichten* **325**, 565–567 (2004).
93. Barkaoui, K. *et al.* Discovery of Three New Transiting Hot Jupiters: WASP-161 b, WASP-163 b, and WASP-170 b. *Astron. J.* **157**, 43 (2019). [1807.06548](https://arxiv.org/abs/1807.06548).
94. Burdanov, A. Y. *et al.* SPECULOOS Northern Observatory: Searching for Red Worlds in the Northern Skies. *Publ. Astron. Soc. Pacific* **134**, 105001 (2022). [2209.09112](https://arxiv.org/abs/2209.09112).
95. Demory, B. O. *et al.* A super-Earth and a sub-Neptune orbiting the bright, quiet M3 dwarf TOI-1266. *Astron. Astrophys.* **642**, A49 (2020). [2009.04317](https://arxiv.org/abs/2009.04317).
96. Stumpe, M. C. *et al.* Kepler Presearch Data Conditioning I—Architecture and Algorithms for Error Correction in Kepler Light Curves. *Publ. Astron. Soc. Pacific* **124**, 985 (2012). [1203.1382](https://arxiv.org/abs/1203.1382).
97. Smith, J. C. *et al.* Kepler Presearch Data Conditioning II - A Bayesian Approach to Systematic Error Correction. *Publ. Astron. Soc. Pacific* **124**, 1000 (2012). [1203.1383](https://arxiv.org/abs/1203.1383).
98. Stumpe, M. C. *et al.* Multiscale systematic error correction via wavelet-based bandsplitting in kepler data. *Publications of the Astronomical Society of the Pacific* **126**, 100 (2014). URL <https://dx.doi.org/10.1086/674989>.
99. Zechmeister, M. & Kürster, M. The generalised Lomb-Scargle periodogram. A new formalism for the floating-mean and Keplerian periodograms. *Astron. Astrophys.* **496**, 577–584 (2009). [0901.2573](https://arxiv.org/abs/0901.2573).

100. Doyle, A. P., Davies, G. R., Smalley, B., Chaplin, W. J. & Elsworth, Y. Determining stellar macroturbulence using asteroseismic rotational velocities from Kepler. *Monthly Notices of the Royal Astronomical Society* **444**, 3592–3602 (2014). URL <https://doi.org/10.1093/mnras/stu1692>. <https://academic.oup.com/mnras/article-pdf/444/4/3592/6344008/stu1692.pdf>.
101. Bruntt, H. *et al.* Accurate fundamental parameters for 23 bright solar-type stars. *Monthly Notices of the Royal Astronomical Society* **405**, 1907–1923 (2010). URL <https://doi.org/10.1111/j.1365-2966.2010.16575.x>. <https://academic.oup.com/mnras/article-pdf/405/3/1907/17324571/mnras0405-1907.pdf>.
102. Gray, R. O. & Corbally, C. J. An Expert Computer Program for Classifying Stars on the MK Spectral Classification System. *Astron. J.* **147**, 80 (2014).
103. Eastman, J., Gaudi, B. S. & Agol, E. EXOFAST: A Fast Exoplanetary Fitting Suite in IDL. *Publ. Astron. Soc. Pacific* **125**, 83 (2013). [1206.5798](https://doi.org/10.1086/67998).
104. Gelman, A. & Rubin, D. B. Inference from Iterative Simulation Using Multiple Sequences. *Statistical Science* **7**, 457–472 (1992).
105. Gelman, A., Carlin, J. B., Stern, H. S. & Rubin, D. B. *Bayesian Data Analysis* (London: Chapman & Hall, 2003), 2 edn.
106. Stassun, K. G. & Torres, G. Evidence for a Systematic Offset of $-80 \mu\text{as}$ in the Gaia DR2 Parallaxes. *Astrophys. J.* **862**, 61 (2018). [1805.03526](https://doi.org/10.3847/1538-4357/aa9999).
107. Schlafly, E. F. & Finkbeiner, D. P. Measuring Reddening with Sloan Digital Sky Survey Stellar Spectra and Recalibrating SFD. *Astrophys. J.* **737**, 103 (2011). [1012.4804](https://doi.org/10.1086/112448).
108. Asplund, M., Grevesse, N., Sauval, A. J. & Scott, P. The Chemical Composition of the Sun. *Annual Review of Astronomy and Astrophysics* **47**, 481–522 (2009). [0909.0948](https://doi.org/10.1146/annurev-astro-08-18-07).
109. Schwarz, G. Estimating the dimension of a model. *Ann. Statist.* **6**, 461–464 (1978). URL <https://doi.org/10.1214/aos/1176344136>.
110. Claret, A. & Bloemen, S. Gravity and limb-darkening coefficients for the Kepler, CoRoT, Spitzer, uvby, UBVRIJHK, and Sloan photometric systems. *Astron. Astrophys.* **529**, A75 (2011).
111. Wagenmakers, E.-J. A practical solution to the pervasive problems of p values. *Psychonomic Bulletin & Review* **14**, 779–804 (2007).
112. Chambers, K. C. *et al.* The Pan-STARRS1 Surveys. *arXiv e-prints* arXiv:1612.05560 (2016). [1612.05560](https://arxiv.org/abs/1612.05560).

Acknowledgments WASP-South is hosted by the South African Astronomical Observatory and we are grateful for their ongoing support and assistance. Funding for WASP comes from consortium universities and from the UK’s Science and Technology Facilities Council. The research leading to these results has received funding from the European Research Council (ERC) under the FP/2007–2013 ERC grant agreement no. 336480, and under the H2020 ERC grant agreement no. 679030; and from an Actions de Recherche Concertée (ARC) grant, financed by the Wallonia-Brussels Federation. The Euler Swiss telescope by the Swiss National Science Foundation (SNF). This work has been carried out in part within the framework of the NCCR PlanetS supported by the Swiss National Science Foundation. This study is based on observations collected at the European Southern Observatory under ESO programme 0102.C-0414, PI: Nielsen. TRAPPIST-South is funded by the Belgian National Fund for Scientific Research (F.R.S.-FNRS) under grant PDR T.0120.21, with the participation of the Swiss National Science Foundation (SNF). M.G. and E.J. are FNRS Senior Research Associates. The postdoctoral fellowship of KB is funded by F.R.S.-FNRS grant T.0109.20 and by the Francqui Foundation. The ULiege’s contribution to SPECULOOS has received funding from the European Research Council under the European Union’s Seventh Framework Programme (FP/2007-2013) (grant Agreement n° 336480/SPECULOOS), from the Balzan Prize Foundation, from the Belgian Scientific Research Foundation (F.R.S.-FNRS; grant n° T.0109.20), from the University of Liege, and from the ARC grant for Concerted Research Actions financed by the Wallonia-Brussels Federation. This work is supported by a grant from the Simons Foundation (PI Queloz, grant number 327127). J.d.W. and MIT gratefully acknowledge financial support from the Heising-Simons Foundation, Dr. and Mrs. Colin Masson and Dr. Peter A. Gilman for Artemis, the first telescope of the SPECULOOS network situated in Tenerife, Spain. This work is supported by the Swiss National Science Foundation (PP00P2-163967, PP00P2-190080 and the National Centre for Competence in Research PlanetS). This work has received fund from the European Research Council (ERC) under the European Union’s Horizon 2020 research and innovation programme (grant agreement n° 803193/BEBOP), from the MERAC foundation, and from the Science and Technology Facilities Council (STFC; grant n° ST/S00193X/1). C.D. was supported by the Swiss National Science Foundation (SNSF) under grant PZ00P2_174028. M.L. acknowledges support of the Swiss National Science Foundation under grant number PCEFP2_194576. E. D acknowledges support from the innovation and research Horizon 2020 program in the context of the Marie Skłodowska-Curie subvention 945298. F.J.P. acknowledges financial support from the grant CEX2021-001131-S funded by MCIN/AEI/10.13039/501100011033.

Author contributions K.B. led the project and performed and interpreted the global analyses with support from F.J.P. and M.G. F.J.P. coordinated the interpretation of the results and writing of the paper. P.N. and J.d.W. performed the assessment of atmospheric-characterization suitability. C.H., O.T., D.R.A., S.U., R.G.W. performed the WASP-South observation and data reduction. C.D., R.H., S.H. performed planet interior models and interpretation of the results. B.S., V.V.G., P.F.L.M., A.S., M.G. performed spectroscopic data, stellar evolutionary models and SED analysis. L.D.N., F.B, M.L. performed Radial velocity measure-

ments. E.J., E.D., C.A.M., P.P.P. performed photometric follow-up using TRAPPIST-South and SPECULOOS-South facilities, and data reduction using Prose. All co-authors read and commented the manuscript, and helped with its revision.

Competing Interests The authors declare no competing interests.

Correspondence Correspondence and requests for materials should be addressed to K.B. (khalid.barkaoui@uliege.be) and F.J.P. (pozuelos@iaa.es).

Facility WASP-South, TRAPPIST-South, SPECULOOS-South, TESS, CORALIE, and HARPS.

Softwares *Matplotlib*⁶¹, *Numpy*⁶², *Astropy*⁶³, *SciPy*⁶⁴, *Lightkurve*⁶⁵, *Prose*⁶⁶, *Wotan*⁶⁷, *Photutils*⁶⁸, *EXOFATSv2*¹⁶, *petitRADTRANS*⁶⁹, *BAGEMASS*⁷⁰, *MCMC*¹⁹

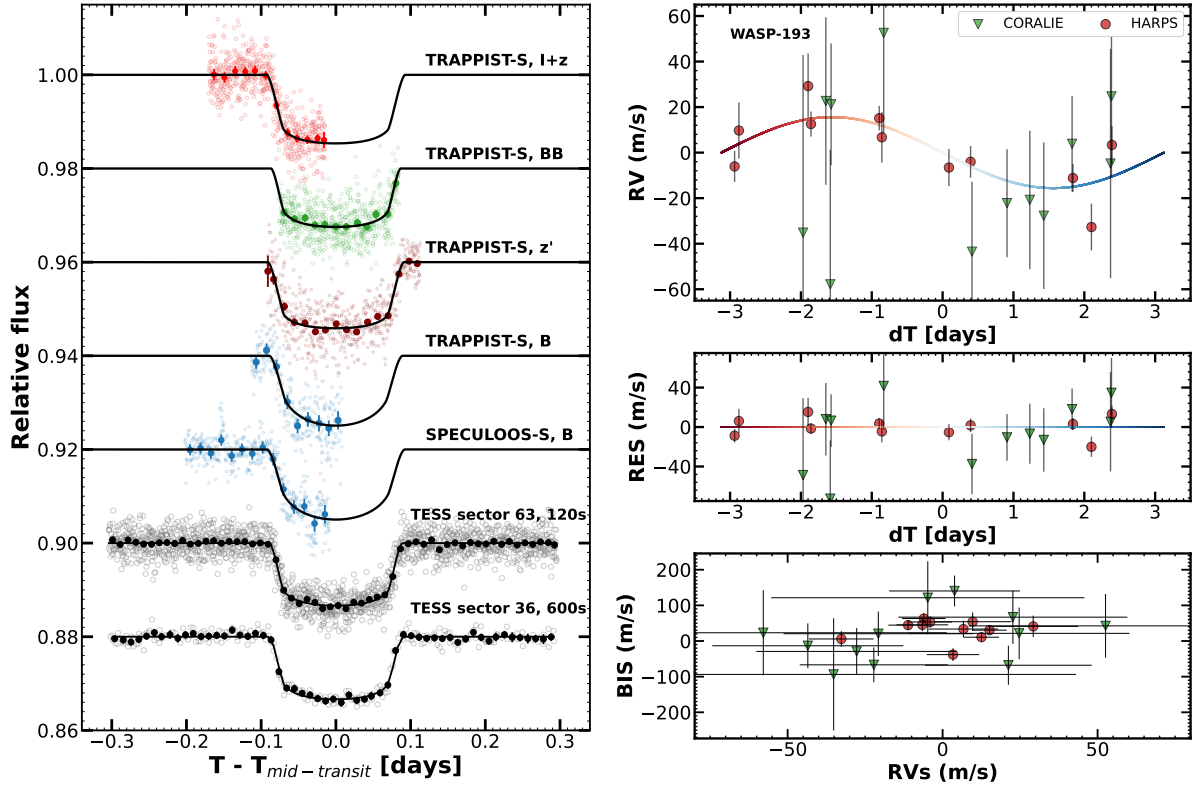


Figure 1: *Left panel:* Follow-up transit photometry of WASP-193 b. Four transits were observed by TRAPPIST-South, one by SPECULOOS-South, and the observations performed by *TESS* in Sector 36 and 63 with 10 and 2-min cadences, respectively. In all the cases, the period-folded is displayed using the best-fitting transit ephemeris deduced from our global MCMC analysis. Each transit light curve has been corrected by the baseline model presented in Table 4. The coloured points with error bars are data binned to 20 min, and the best-fitting model is superimposed in black. *Top right panel:* RVs obtained with the CORALIE and HARPS spectrographs for WASP-193 period-folded using the best-fitting orbital model, which is superimposed as a solid line (in $m s^{-1}$). RVs color line of the best fitting shows the Doppler effect. *Middle right panel:* RV residuals of the fit (in $m s^{-1}$). The coloured triangles and circles correspond to the CORALIE and the HARPS data, respectively. *Bottom right panel:* Bisector-span as a function of RV (in $m s^{-1}$) of WASP-193 obtained with the CORALIE and HARPS spectrographs. We assumed that the bisector-span error bars as twice the RV error bars^{71–73}. There is no significant correlation between the bisector-spans and RVs (the resulting Pearson r coefficient was found to be $r_{\text{HARPS}} = 0.07$ for HARPS and $r_{\text{CORALIE}} = 0.21$ for CORALIE); therefore, the Pearson coefficient supports no significant correlation between RVs and BIS.

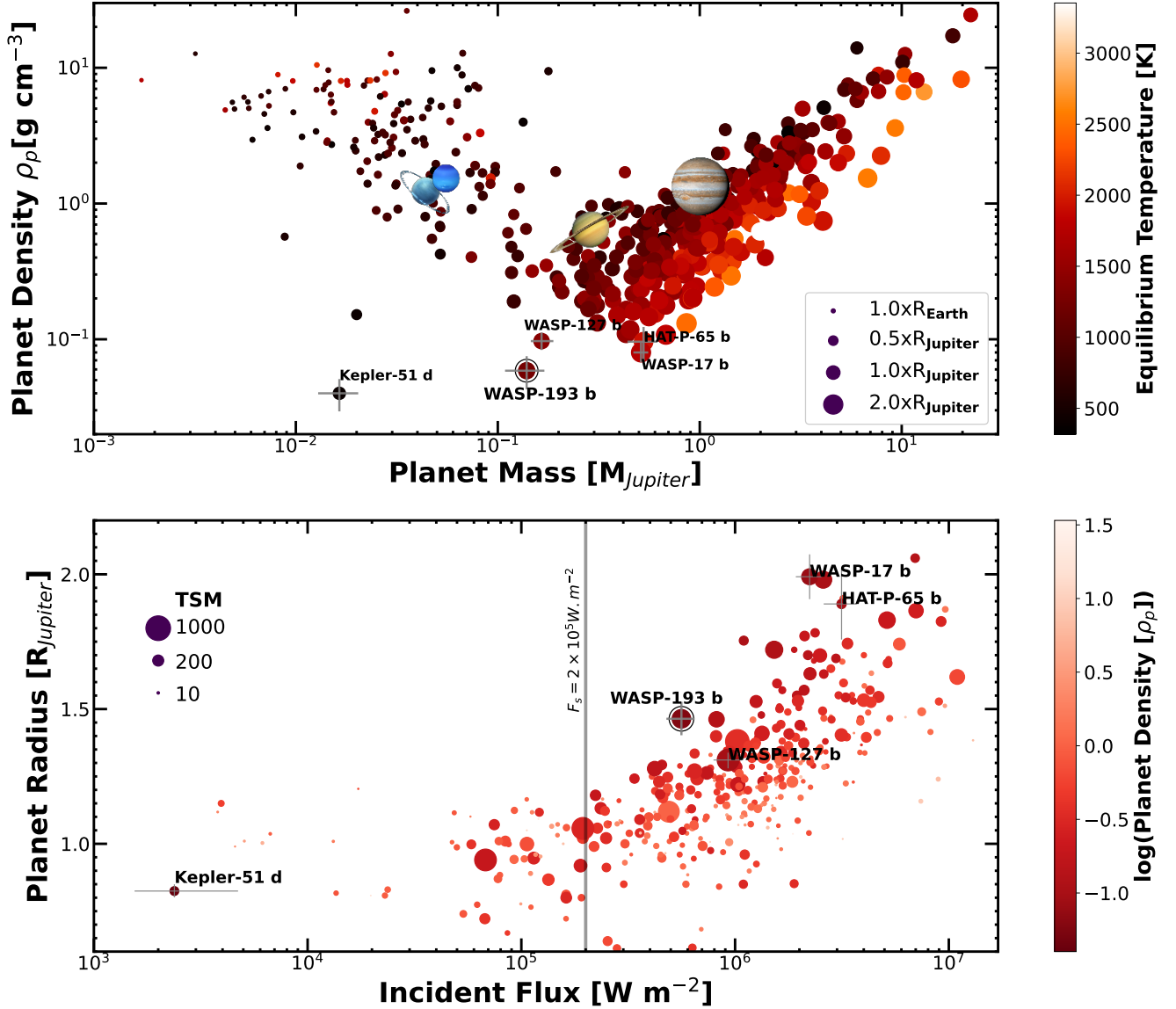


Figure 2: Planetary diagrams of known transiting exoplanets obtained from *NASA Archive of Exoplanets* with radius and mass precisions better than 8% and 25%, respectively. *Top panel*: Planetary density as a function of the planetary mass. The size of the points scale with the planetary radius. The points are coloured according to their equilibrium temperature. WASP-193 b and the least dense planets known to date are labelled and displayed with their 1σ uncertainties (Kepler-51 d⁷⁴, WASP-17 b⁷⁵, WASP-127 b⁷⁶ and HAT-P-65 b⁷⁷). *Bottom panel*: Planetary radius as a function of the stellar incident flux. The size of the points scale with the TSM¹. The points are coloured according to their planetary density. The radii begin to show a correlation with stellar incident fluxes at $\sim 2 \times 10^5 \text{ W m}^{-2}$ (vertical gray line)⁷⁸.

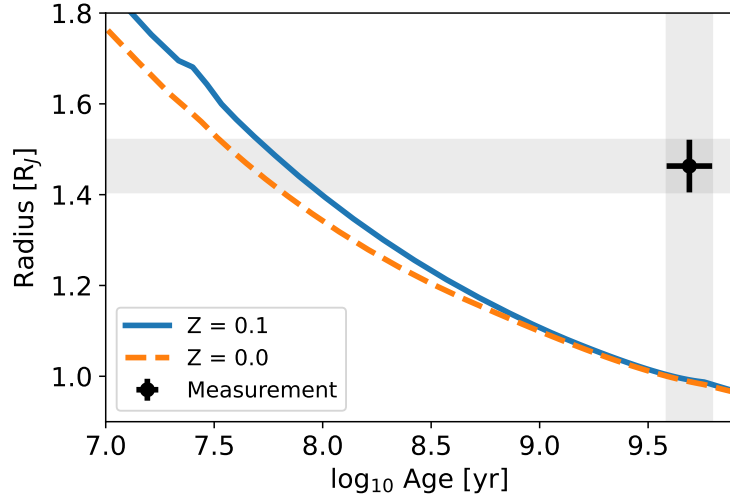


Figure 3: Planetary Radius as a function of age for two evolution models. The orange dashed line and solid blue lines are for $Z = 0.0$ and 0.1 , respectively. The radius and age inferred from observations are shown as the black error bars and the grey-shaded regions. The radius evolution of the planet includes the effect of the evolving stellar irradiation (see text for details). Note that the slow cooling of the model with $Z = 0.1$ allows for larger radii compared to a pure H-He composition.

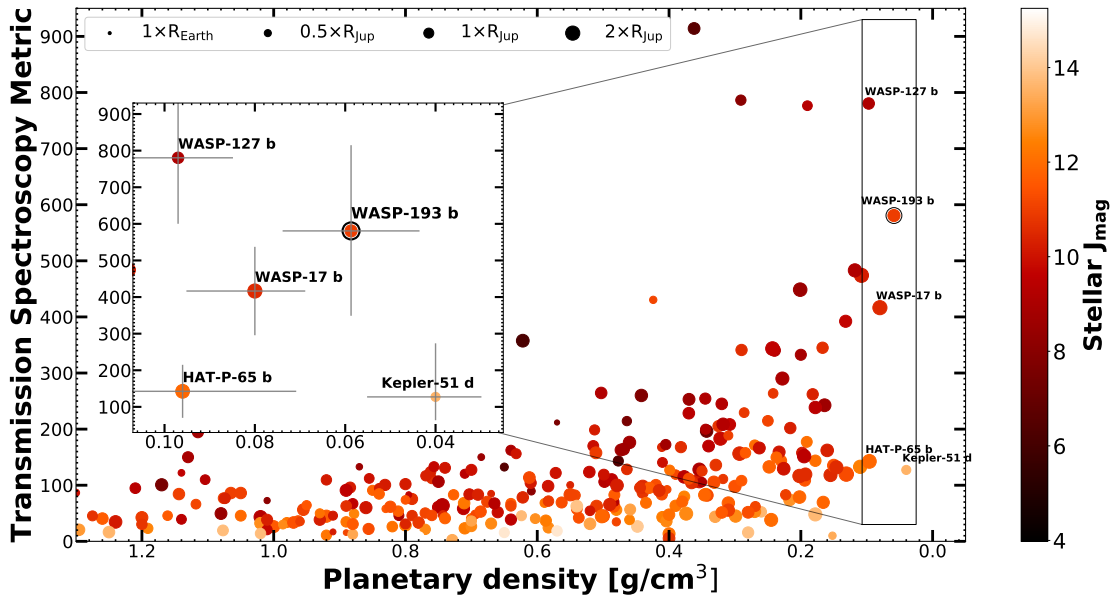


Figure 4: Feasibility of WASP-193 b for transmission spectroscopy studies. The transmission spectroscopy metric (TSM) is presented as a function of the planetary density of known transiting exoplanets obtained from the [NASA Exoplanet Archive](#) with radius and mass precisions better than 8% and 25%, respectively. The point size scales with the planetary radius. The points are coloured according to the host star J_{mag} . The black circle highlights WASP-193 b.

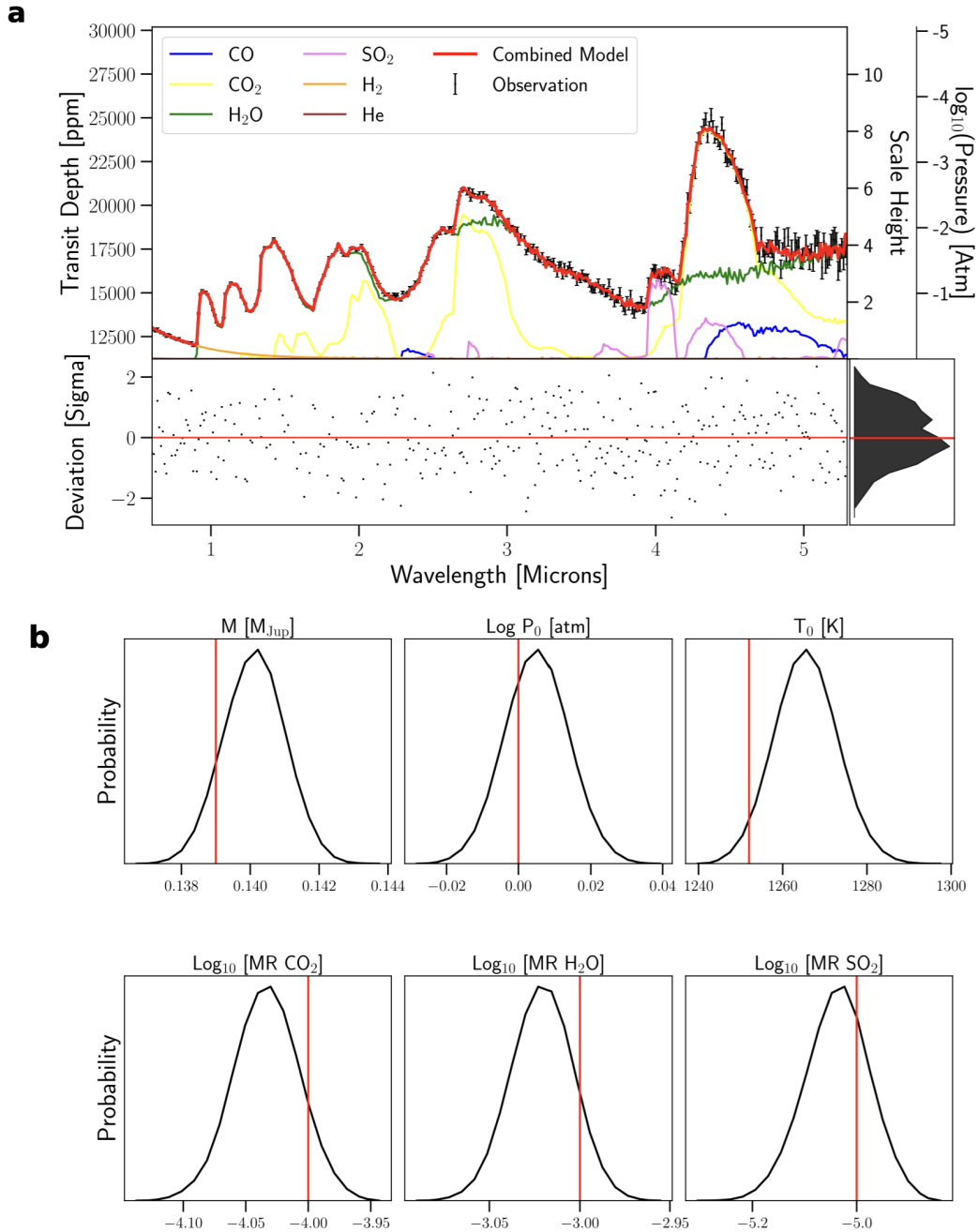


Figure 5: WASP-193 b as an exquisite target for atmospheric characterization. **a.** Synthetic transmission spectrum model and best-fit model for the injection-retrieval test for a single JWST/NIRSpec/Prism transit of WASP-193 b. Models and tests are produced with TIERRA pipeline⁵². **b.** Posterior probability distributions of the key planetary properties retrieved showcasing that one single JWST visit can yield the constraints on the main atmospheric properties and the planetary mass within ~ 0.1 dex and $\sim 1\%$, respectively.

Star information		
Parameter	WASP-193	Source
Identifying information:		
WASP ID	1SWASPJ105723.88-295949.6	
GAIA DR3 ID	5453063823882876032	Ref. 15
TESS ID	TIC 49043968	Ref. 79
2MASS ID	10572385-2959497	Ref. 80
RA [J2000]	$10^h 57^m 23.85^s$	Ref. 15
Dec [J2000]	$-29^\circ 59' 49.66''$	Ref. 15
Parallax and distance:		
Plx [<i>mas</i>]	2.648 ± 0.015	Ref. 15
Distance [pc]	377.72 ± 2.17	Ref. 15
Photometric properties:		
V_{mag} [APASS]	12.19 ± 0.09	Ref. 81
B_{mag} [APASS]	12.72 ± 0.03	Ref. 81
G_{mag} [Gaia_DR3]	12.033 ± 0.003	Ref. 15
J_{mag} [2MASS]	10.95	Ref. 80
H_{mag} [2MASS]	10.81 ± 0.03	Ref. 80
K_{mag} [2MASS]	10.75 ± 0.04	Ref. 80
TESS _{mag}	11.63 ± 0.01	Ref. 79
$W1_{\text{mag}}$ [WISE]	10.64 ± 0.03	Ref. 82
$W2_{\text{mag}}$ [WISE]	10.68 ± 0.03	Ref. 82
$W3_{\text{mag}}$ [WISE]	10.49 ± 0.09	Ref. 82
Stellar parameters from spectroscopic analysis		
T_{eff} [K]	6076 ± 120	This work (section 1)
$\log g_*$ [dex]	4.1 ± 0.1	This work (section 1)
$\log(R'_{hk})$ [dex]	5.30 ± 0.07	This work (section 1)
$[Fe/H]$ [dex]	-0.06 ± 0.09	This work (section 1)
$V \sin(i)$ [km/s]	4.3 ± 0.8	This work (section 1)
v_{macro} [km/s]	4.45	This work (section 1)
v_{micro} [km/s]	1.17	This work (section 1)
Spectral type	F9	This work (section 1)
Stellar parameters from SED and CLES analysis		
T_{eff} [K]	6080^{+90}_{-98}	EXOFASTv2 (This work section 1)
$[Fe/H]$	-0.193 ± 0.086	EXOFASTv2 (This work section 1)
M_* [M_\odot]	1.120 ± 0.051	EXOFASTv2 (This work section 1)
M_* [M_\odot]	1.102 ± 0.070	CLES (This work section 1)
R_* [R_\odot]	$1.225^{+0.032}_{-0.029}$	EXOFASTv2 (This work section 1)
L_* [L_\odot]	$1.65^{+0.13}_{-0.12}$	EXOFASTv2 (This work section 1)
Age [Gyr]	4.4 ± 1.9	CLES (This work section 1)
Age [Gyr]	6.6 ± 2.4	EXOFASTv2 (This work section 1)

Table 1: Stellar properties of WASP-193 derived from astrometry, photometry, spectroscopy, SED and CLES analysis.

Parameter	Symbol	Value	Value	Unit
		(Circular, $e = 0$)	(Eccentric, $e \neq 0$)	
<i>Deduced stellar parameters</i>		WASP-193		
Mean density	ρ_\star	$0.567^{+0.051}_{-0.048}$	$0.557^{+0.051}_{-0.047}$	ρ_\odot
Stellar mass	M_\star	1.068 ± 0.066	$1.059^{+0.067}_{-0.068}$	M_\odot
Stellar radius	R_\star	1.235 ± 0.027	1.239 ± 0.028	R_\odot
Luminosity	L_\star	$1.87^{+0.18}_{-0.16}$	$1.88^{+0.18}_{-0.16}$	L_\odot
<i>Deduced planet parameters</i>		WASP-193 b		
Scaled semi-major axis	a/R_\star	11.81 ± 0.34	$11.74^{+0.35}_{-0.34}$	R_\star
Orbital semi-major axis	a	0.0678 ± 0.0014	0.0676 ± 0.0015	au
Orbital inclination	i_p	$88.51^{+0.57}_{-0.43}$	$88.49^{+0.78}_{-0.49}$	deg
Eccentricity	e	0 (fixed)	$0.056^{+0.068}_{-0.040}$	–
Density	ρ_p	$0.059^{+0.015}_{-0.014}$	$0.059^{+0.015}_{-0.013}$	g cm^{-3}
Surface gravity	$\log g_p$	$2.23^{+0.09}_{-0.11}$	$2.22^{+0.09}_{-0.11}$	cgs
Mass	M_p	$0.141^{+0.029}_{-0.030}$	0.139 ± 0.029	M_{Jup}
Radius	R_p	$1.463^{+0.059}_{-0.057}$	$1.464^{+0.059}_{-0.057}$	R_{Jup}
Equilibrium temperature	T_{eq}	1252 ± 30	1254 ± 31	K
Irradiation	S_p	$5.58^{+0.57}_{-0.52} \times 10^5$	$5.62^{+0.53}_{-0.57} \times 10^5$	Wm^{-2}
Bayesian Information Criterion	BIC	2324	2318	–

Table 2: The WASP-193 system parameters derived from our global MCMC analysis (medians and 1σ limits of the marginalized posterior probability distributions).

1 Methods

WASP observations and data reduction The Super-WASP (Wide Angle Search for Planets³) project consists of data obtained at telescopes located at two sites: Sutherland Station of the South African Astronomical Observatory (SAAO) and the Observatorio del Roque de los Muchachos on the island of La Palma in the Canary Islands. The field-of-view (FOV) of each instrument is 482 deg^2 with a pixel scale of $13.7'' \text{ pixel}^{-1}$. These instruments are capable of obtaining photometry with a precision better than 1% for objects with V -magnitudes between 7.0 and 11.5³. The WASP ground-based transit survey has discovered almost 200 planets, transiting bright nearby stars, mostly hot Jupiters plus minor fraction of short-period Saturn- and Neptune-mass objects.

Many WASP planets have proven to be among the most favorable targets for detailed atmospheric characterization with current facilities such as the *HST*⁸³, *VLT*⁸⁴, *Magellan*⁸⁵, and *JWST*⁸⁶ (e.g., WASP-17 b⁸⁷, WASP-101 b⁸⁸, WASP-121 b⁸⁹ and WASP-127 b⁹⁰). The hot-star WASP-193* was observed by the WASP-South survey in 2006 and 2012. The WASP data calibration (bias and dark subtraction, and flat-field division) was performed using a bespoke pipeline⁹¹ developed in Fortran. Aperture photometry was performed on the final calibrated images, where the stars' fluxes were measured in three photometric apertures with radii of 2.5, 3.5, and 4.5 pixels, following the method described by ref.^{3,91,92}. The WASP phase-folded light curve obtained for WASP-193 is presented in Figure 6. The search for transit events in the WASP photometry was conducted employing the Box-Least-Square (BLS) method as described in ref.⁹¹. The alert for this candidate triggered the ground-based follow-up campaign using both photometry and spectroscopy measurements to confirm the planetary nature of the detected signal.

TRAPPIST-South photometry TRAPPIST (TRAnsiting Planets and Planetesimals Small Telescope) network is composed of the 0.6-m twin robotic telescopes TRAPPIST-South and TRAPPIST-North^{4,5,93}. For WASP-193, we used TRAPPIST-South located at the La Silla observatory in Chile. It is equipped with a thermo-electrically 2K×2K FLI ProLine PL3041-BB CCD camera with a FOV of $22' \times 22'$ and a pixel scale of $0.65''$ per pixel. TRAPPIST-South observed a full transit of WASP-193 b in the Sloan- z' filter on 27 January 2017 with an exposure time of 20s, three partial transits, one in the $I+z$ filter on 02 January 2015 with an exposure time of 10s, one in the BB filter on 06 April 2015 with an exposure time of 8s, and a last one in the Johnson- B filter on 08 June 2019 with an exposure time of 25s. Data calibration and differential photometry were performed using the *PROSE*[†] pipeline⁶⁶. The reduced light curves obtained for WASP-193 are presented in Figure 1.

SPECULOOS-South photometry The SPECULOOS (Search for habitable Planets Eclipsing ULtra-cOOL Stars) robotic telescope network is composed of the SPECULOOS Southern Observatory⁶⁻⁸

*Other stellar designations: 1SWASPJ105723.88-295949.6 = TYC 6647-516-1 = Gaia DR2 5453063823882876032 = 2MASS 10572385-2959497

[†]*PROSE*: <https://github.com/lgrcia/prose>

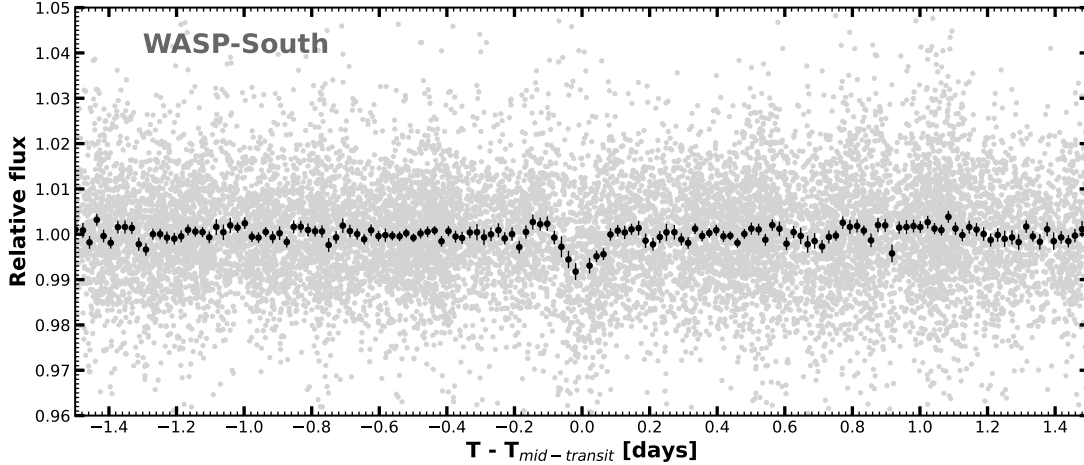


Figure 6: Detrended discovery light-curve of WASP-193 obtained with WASP-South (gray points: unbinned and black points: bin width = 30 min), period-folded using the orbital period deduced from our data analysis.

(SSO), with four 1-m telescopes at ESO Paranal Observatory in Chile and two 1-m telescopes in the Northern hemisphere: the SPECULOOS Northern Observatory⁹⁴ (SNO) at Teide Observatory in Spain and SAINT-EX⁹⁵ (Search And characterIsationN of Transiting EXoplanets) at San Pedro Mártir Observatory in Mexico. These facilities are identical Ritchey-Chretien telescopes equipped with ANDOR iKon-L BEX2-DD cameras and 2048×2088 e2v CCD detectors, with a FOV of $12' \times 12'$ and a pixel scale of $0.35''$ per pixel. We observed a partial transit of WASP-193 b with one of the four telescopes of SSO on 08 June 2019 in the Johnson-*B* filter with an exposure time of 25s. Data calibration and differential photometry were performed using the *PROSE* pipeline⁶⁶. The reduced light curve obtained is presented in Figure 1.

TESS photometry The *TESS* (Transiting Exoplanet Survey Satellite¹¹) mission was launched by NASA in April 2018. Its main goal is to detect and characterise transiting exoplanets smaller than Neptune orbiting nearby bright stars. *TESS*'s combined FOV is $24^\circ \times 96^\circ$, and one pixel is $\sim 21''$ on the sky. WASP-193 was observed by *TESS* with a 30-min cadence in the ninth sector of its primary mission (from 28 February to 26 March 2019), with a 10-min cadence during its extended mission in sector 36 (from 07 March to 02 April 2021) and with 2-min cadence in sector 63 (from 10 March 2023 to 06 April 2023). We retrieved the light curves produced by the TESS Science Processing Operations Center pipeline⁹⁶⁻⁹⁸ (PDC-SAP) corresponding to the 2-min and 10-min cadences from the Mikulski Archive for Space Telescope. These light curves are corrected for instrument systematics and crowding effects.

Spectroscopic and radial-velocity measurements In this paper, we used RV measurements obtained by CORALIE (mounted on the 1.2-m Swiss Euler telescope located at ESO La Silla in Chile⁹) and HARPS (mounted on the 3.6-m telescope at ESO La Silla in Chile¹⁰) spectrographs.

We obtained 12 (between June 2015 and June 2018) and 11 (between February and July 2019) spectroscopic measurements of WASP-193 with the CORALIE and HARPS spectrographs, respectively. We applied the cross-correlation method¹² on the observed spectra of WASP-193 to extract the radial velocity measurements presented in Table 6.

The RV measurements of WASP-193 are in phase with the ephemerides from the WASP-South photometric data, but the planet was not independently detected in the RV data. The offset between RV data sets is taken into account by modeling the systematic velocity for each instrument during the global analysis. The marginally strongest signal in the generalised Lomb-Scargle periodogram⁹⁹ coincided with the transit period of 6.25 days, though the significance was below 10% FAP. The RV measurements obtained with CORALIE and HARPS are presented in Table 6, and the phase-folded RV curve of WASP-193 is presented in Figure 1. The corresponding RV based on the fitting linear slope, enables us to discard the blended eclipsing binary (BEB) scenario and to keep the planetary companion. We calculated the Pearson r coefficient, which measures the correlation between two parameters. The results were consistent with zero, i.e., no correlation; $r_{\text{Harps}} = 0.07$ and $r_{\text{Coralie}} = 0.21$ for HARPS and CORALIE, respectively. Hence, the Pearson r coefficient supported the planetary nature of WASP-193 b.

We used co-added spectra obtained with the HARPS spectrograph to produce a single spectrum with S/N of 75, which allowed us to constrain the stellar atmospheric parameters of WASP-193 better using the method described by ref.¹⁴. The metallicity, $[Fe/H]$, was computed from the Fe lines, the effective temperature, T_{eff} , was computed from the $H\alpha$ line, the surface gravity, $\log g$, was estimated from the Mg Ib and Na ID lines, the activity index, $\log(R'_{hk})$, was constrained from the Ca II H+K lines and the rotational velocity, $V \sin(i)$, was measured by assuming a macroturbulence value of $v_{\text{macro}} = 4.45 \text{ km s}^{-1}$, which was extracted from the calibration formula¹⁰⁰, and a microturbulence value of $v_{\text{micro}} = 1.17 \text{ km s}^{-1}$, which was extracted from the calibration formula¹⁰¹. With these values, it was found that WASP-193 is a Sun-like star with $T_{\text{eff}} = 6076 \pm 120 \text{ K}$, $\log g_{\star} = 4.1 \pm 0.1 \text{ dex}$, $[Fe/H] = -0.06 \pm 0.09 \text{ dex}$, $V \sin(i) = 4.3 \pm 0.8 \text{ km s}^{-1}$, and $\log(R'_{hk}) = 5.30 \pm 0.07 \text{ [dex]}$. Using the *MKCLASS*[‡] program¹⁰², we got a spectral-type of F9 from the observed HARPS spectrum. This is consistent with that estimated from the stellar atmospheric parameters and $B - V$ color index.

Stellar parameters from the *ExoFASTv2* analysis As an independent check of the derived stellar parameters for WASP-193, we performed an analysis using the exoplanet fitting suite, *EXOFASTv2*^{16,103}. *EXOFASTv2* uses a differential evolution MCMC to globally and simultaneously model the star and planet. The built-in Gelman–Rubin statistic^{104,105} is used to check the convergence of the chains. A full description of *EXOFASTv2* was given by ref.¹⁶.

Within the fit, the host star’s parameters are determined using the SEDs (see Figure 7) con-

[‡]*MKCLASS*: <http://www.apstate.edu/~grayro/mkclass/>

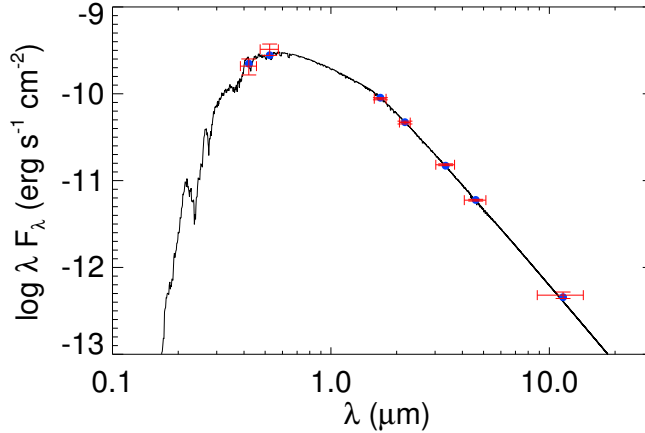


Figure 7: SED model (black line) of WASP-193 and the *EXOFASTv2* fit with broads and averages (blue circles) and broadband measurements (red). The error bars in wavelength denote the bandwidth of the corresponding filter and the error bars in flux denote the measurement uncertainties.

constructed from our broadband photometry, MESA Isochrones and Stellar Tracks (MIST) evolutionary models^{35,36}. For the SED fits performed within *EXOFASTv2*, we used photometry from APASS DR9 BV⁸¹, 2MASS HK⁸⁰, and ALL-WISE W1, W2 and W3⁸², which are presented in Table 1.

We applied Gaussian priors to the parameters T_{eff} , $\log g_*$, and $[Fe/H]$ using the obtained values from the spectroscopic analysis (Section 1). We also enforced Gaussian priors on the Gaia DR3¹⁵ parallax (adding $82 \mu\text{as}$ to the reported value and adding $33 \mu\text{as}$ in quadrature to the error, following the recommendation of ref.¹⁰⁶). We adopted an upper limit on the extinction of $A_V = 0.20$ from ref.¹⁰⁷ using their web interface.[§] The results of *EXOFASTv2* fit are presented in Table 1.

Stellar parameters using *CLES* We used our Liège stellar evolution code, *CLES*, to determine the age and mass of the host star. All the details concerning the input physics (treatment of convection, surface boundary conditions, nuclear reaction rates, equation of state, opacities, and diffusion) can be found in Sect. 2.3 of ref.¹⁸. We adopted the solar mixture of ref.¹⁰⁸. As inputs, we used the spectroscopic T_{eff} and $[Fe/H]$, as well as the stellar radius R_* obtained from SED-fitting using *ExoFASTv2*[¶]. We computed stellar evolutionary tracks and selected the best-fit one according to the input parameters following the Levenberg-Marquadt minimisation scheme, as explained in ref.¹⁸. We obtained $M_* = 1.102 \pm 0.070 M_\odot$ and $t_* = 4.4 \pm 1.9 \text{ Gyr}$ (see Table 1).

[§] <https://irsa.ipac.caltech.edu/applications/DUST/>

[¶]Very similar results are obtained adopting instead the luminosity L_* obtained from bolometric flux (again by SED-fitting) and distance, or the stellar density derived from transit light curves.

Modelling of the spectroscopic and photometric data We combined the spectroscopic and photometric observations of WASP-193 to determine the physical parameters of the planetary system. The stellar atmospheric parameters, T_{eff} , $\log g_*$ and $[Fe/H]$ from our spectroscopic analysis, were coupled with the stellar radius R_* obtained from *EXOFASTv2* (section 1) and mass M_* obtained from *CLES* (see section 1) analysis to infer the stellar density, ρ_* , luminosity, L_* , and other physical parameters.

We used a Markov-chain Monte Carlo (MCMC) algorithm¹⁹ to sample the posterior probability distributions of the system’s parameters, from which we extracted the median values and their 1σ -uncertainties. All photometric measurements contain additional faint ($G_{\text{mag}} \sim 16$) neighbour star at $4.2''$ (see Figure 8). The resulting dilution was found to be $< 5\%$, which is included in our global analysis.

We modelled the RV curves using a 2-body Keplerian model²¹ shown in Table 6, and the transit light curves using the Mandel & Agol²⁰ model multiplied by a baseline to correct for several external effects related to time, full-width half-maximum (FWHM), airmass, position dx, dy and background (see Table 4). The baseline model for each transit light curve was selected based on minimizing the Bayesian information criterion (BIC)¹⁰⁹ using the formula:

$$BIC = \chi^2 + k \log(N), \quad (1)$$

where k is the number of free parameters, N is the number of data points, and $\chi^2 = -2 \log(L)$, L is the maximized value of the model’s likelihood function. The light curve observed on 06 April 2015 with TRAPPIST-South contains a meridian flip (i.e., a 180° rotation that the German equatorial mount has to undergo when the target star passes the local meridian) at $\text{BJD} = 2457119.619198$ (see details in Table 4), that we modeled as a flux offset in our MCMC analysis.

The jump parameters in our MCMC analysis (i.e., parameters randomly perturbed at each step of the MCMC) were:

- T_0 : the transit timing;
- W : the total duration of the transit (i.e. duration between ingress and egress);
- $dF = R_p^2/R_*^2$: the transit depth, where R_p and R_* are the planetary and stellar radii, respectively;
- $b' = a \cos(i)/R_*$: the impact parameter, where i is the orbital inclination and a is the orbital semi-major axis;
- P : the orbital period;

- $K_2 = K P^{1/3} \sqrt{1 - e^2}$, where K is the semi-amplitude of the RV and e is the orbital eccentricity; and
- $\sqrt{e} \cos(w)$ and $\sqrt{e} \sin(w)$, where w is the argument of periastron.

The stellar parameters T_{eff} , $[Fe/H]$, and M_{\star} were also jump parameters in our analysis. For T_{eff} , $[Fe/H]$, and $\log g_{\star}$, we applied Gaussian priors based on the results of our spectroscopic analysis.

We assumed a quadratic limb-darkening (LD) law to take into account the impact of limb-darkening on our transit light curves. For each filter, the quadratic LD coefficients, u_1 and u_2 , were interpolated from the tables of ref.¹¹⁰ using the T_{eff} , $\log g_{\star}$ and $[Fe/H]$, obtained from our spectroscopic analysis. For the non-standard $I + z$ and BB filters, we took the averages of the values for the standard filters Ic and Sloan- z' for the $I + z$ filter, and Ic and Johnson- R for the BB filter. The LD coefficient values of u_1 and u_2 for each filter are presented in Table 3.

We performed two independent MCMC analyses: one assuming a circular orbit (model 1) and the other assuming an eccentric orbit (model 2). For each model, we calculated the BIC value, which was then used to compute the Bayes Factor (BF) using the relationship described by ref.¹¹¹. The Bayes Factor (BF_{12}) was determined as $\text{BF}_{12} = e^{(BIC_{\text{model}2} - BIC_{\text{model}1})/2}$. Our analysis yielded a BF_{12} value of 20.1, indicating strong evidence in favor of the eccentric scenario¹¹¹.

For each transit light curve, a preliminary MCMC analysis composed of one Markov chain of 100 000 steps was performed to estimate the correction factor (CF) to rescale the photometric errors by $CF = \beta_{\text{red}} \times \beta_{\text{white}}$, where β_{red} is the red noise and β_{white} is the white noise, as described by ref.¹⁹. For the RVs, a *jitter* noise (i.e., the quadratic difference between the mean error of the measurements and the standard deviation of the best-fitting residuals) of 22.3 m s^{-1} for CORALIE and 4.1 m s^{-1} for HARPS was added quadratically to the RV error bars. Then, we conducted a global MCMC analysis composed of five chains of 100 000 steps. The convergence of each chain was checked using the statistical test presented by Gelman-Rubin¹⁰⁴. The deduced parameters of the WASP-193 system are presented in Table 2.

Atmospheric model and injection-retrieval test

The atmospheric model and the injection-retrieval test performed to assess WASP-193 b's suitability for atmospheric exploration with JWST uses the TIERRA retrieval framework⁵². We model a synthetic WASP-193 b atmosphere using abundances consistent with WASP-39 b (volume mixing ratio of $\text{CO}: 10^{-5}$, $\text{CO}_2: 10^{-4}$, $\text{H}_2\text{O}: 10^{-3}$, $\text{SO}_2: 10^{-5}$). We tested four different instrumental settings (NIRSpec Grism, NIRISS SOSS, NIRCAM F322W2, and NIRSpec G395H) and found that while all lead constraints on the planetary properties, *JWST/NIRSpec* Prism provides the most comprehensive constraints owing to its more extensive wavelength coverage. Figure 5 presents the synthetic data, the best fit, and the retrieved planetary parameters.

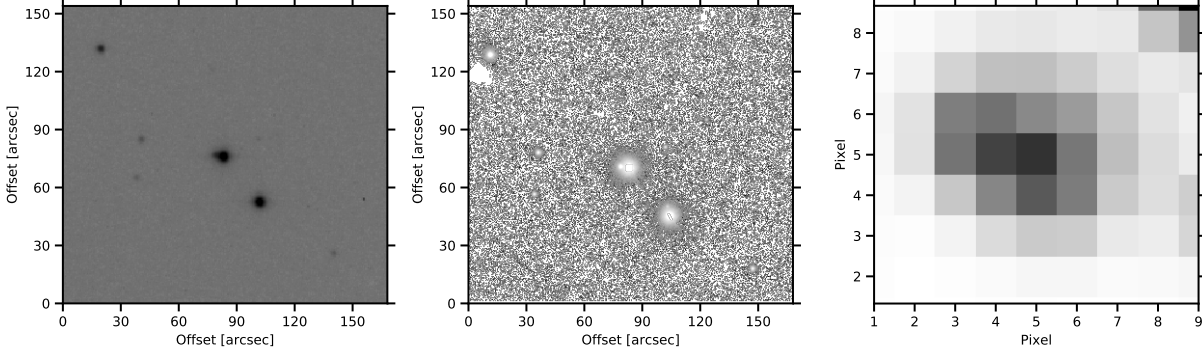


Figure 8: *Left panel:* TRAPPIST-South z' image cropped on a $150 \times 150''$ region around WASP-193. *Middle panel:* Pan-STARRS¹¹² z' image of the same $150 \times 150''$ region around WASP-193 with an image-scale of $0.25'' \text{ pixel}^{-1}$. *Right panel:* TESS $150 \times 150''$ image with the same FOV as the left and middle panels.

Parameter	Value	Prior
Effective temperature T_{eff} [K]	6078 ± 120	$N(6080, 120^2)$
Surface gravity $\log g_*$ [dex]	4.284 ± 0.033	$N(4.1, 0.1^2)$
Rotational velocity $V \sin(i)$ [km/s]	4.29 ± 0.81	$N(4.3, 0.8^2)$
Metallicity $[Fe/H]$ [dex]	-0.060 ± 0.088	$N(-0.06, 0.09^2)$
Stellar mass M_* [M_\odot]	1.059 ± 0.067	$N(1.102, 0.070^2)$
Stellar radius R_* [R_\odot]	1.235 ± 0.027	$N(1.225, 0.032^2)$
Quadratic LD $u_{1,\text{Sloan}-z'}$	0.207 ± 0.013	$N(0.207, 0.013^2)$
Quadratic LD $u_{2,\text{Sloan}-z'}$	9.288 ± 0.065	$N(0.288, 0.007^2)$
Quadratic LD $u_{1,I+z'}$	0.219 ± 0.014	$N(0.224, 0.014^2)$
Quadratic LD $u_{2,I+z'}$	0.290 ± 0.007	$N(0.291, 0.006^2)$
Quadratic LD $u_{1,\text{Johnson}-B}$	0.580 ± 0.027	$N(0.543, 0.026^2)$
Quadratic LD $u_{2,\text{Johnson}-B}$	0.022 ± 0.020	$N(0.209, 0.019^2)$
Quadratic LD $u_{1,\text{Blue}-\text{Blocking}}$	0.275 ± 0.014	$N(0.276, 0.015^2)$
Quadratic LD $u_{2,\text{Blue}-\text{Blocking}}$	0.298 ± 0.006	$N(0.298, 0.064^2)$
Quadratic LD $u_{1,\text{TESS}}$	0.254 ± 0.016	$N(0.252, 0.015^2)$
Quadratic LD $u_{2,\text{TESS}}$	0.296 ± 0.008	$N(0.295, 0.005^2)$

Table 3: Priors used for WASP-193 for final global joint analysis.

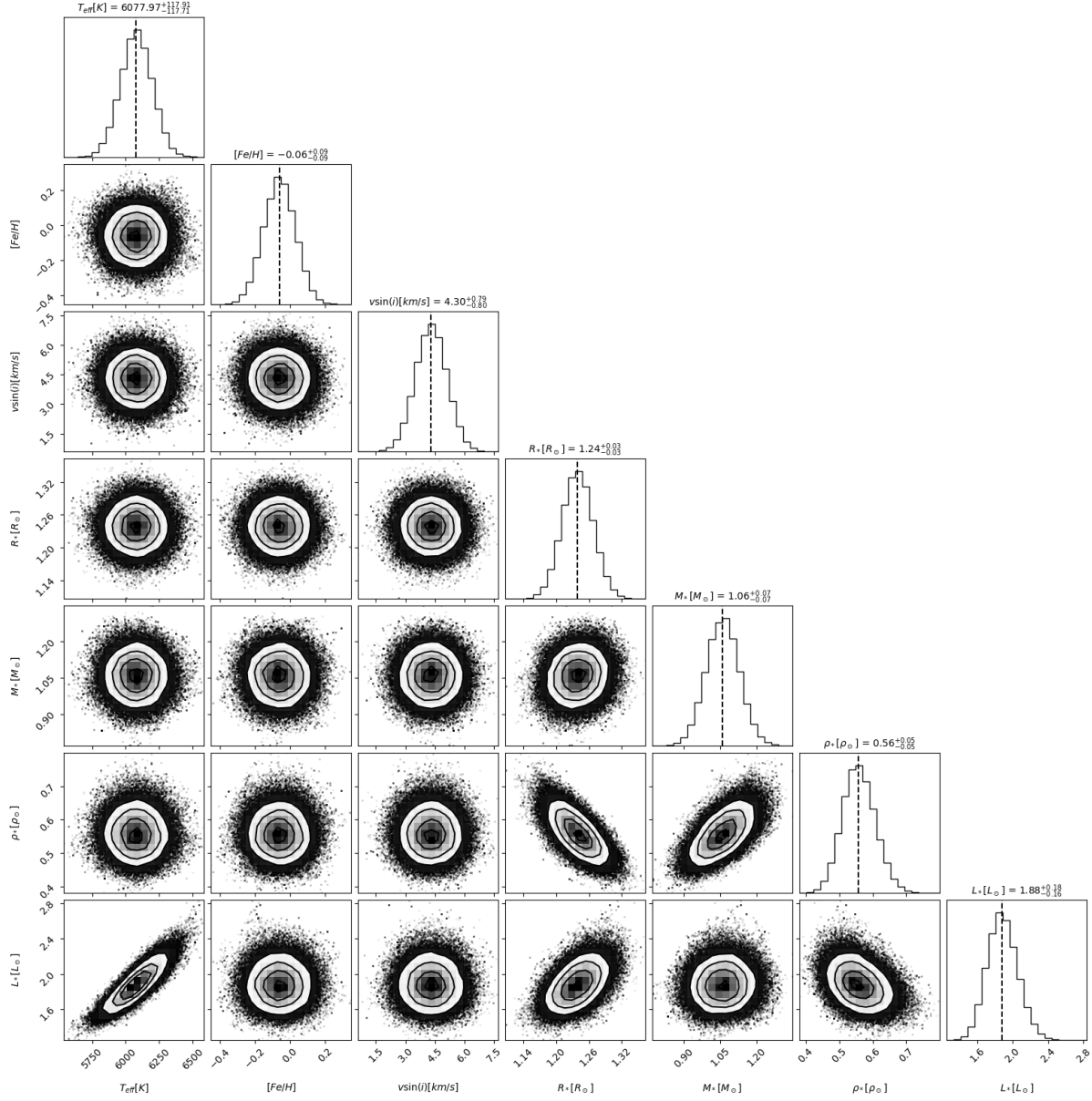


Figure 9: Posterior probability distribution for the stellar physical parameters fitted using our MCMC code as described in Methods. The vertical lines present the median value.

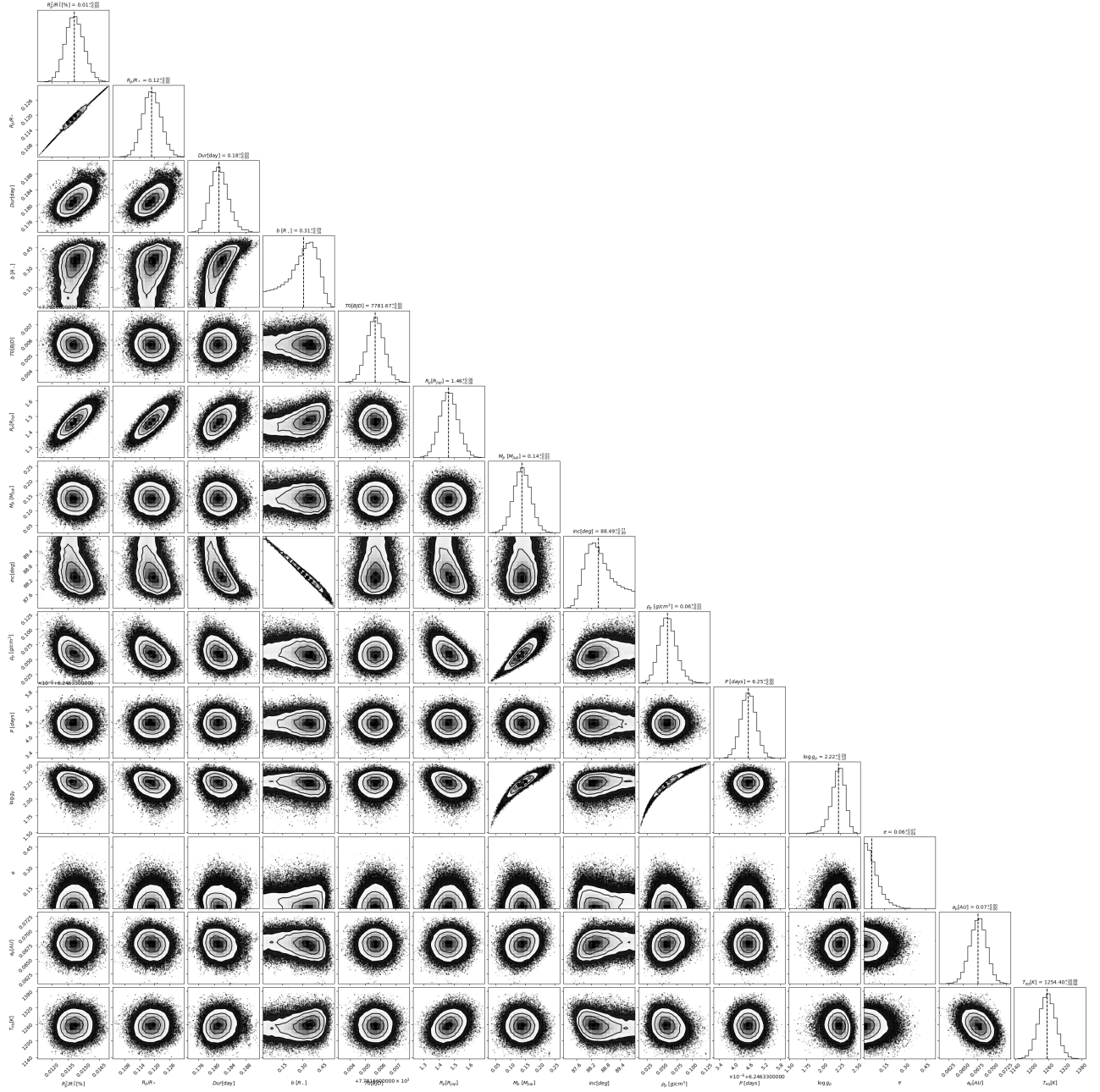


Figure 10: Posterior probability distribution for the planetary physical parameters fitted using our MCMC code as described in Methods. The vertical lines present the median value.

Observation parameters							MCMC analysis				
Telescope	Date	Filter	N_p	$ExpT$ (s)	Duration (min)	$FWHM$ (pixel)	Baseline function	Residual RMS	β_w	β_r	CF
TRAPPIST-S	02 Jan 2015	$I+z$	638	10	224	2.90	$f(t^1, f^1)$	0.0043	1.09	2.27	2.48
TRAPPIST-S	06 Apr 2015	BB	724	8	230	2.67	$f(a^1, O)$	0.0037	0.85	1.65	1.40
TRAPPIST-S	27 Jan 2017	z'	602	20	297	3.28	$f(t^1, b^1)$	0.0042	1.00	1.34	1.34
TRAPPIST-S	08 Jun 2019	B	292	25	176	3.32	$f(t^1, b^1)$	0.0042	0.74	1.60	1.18
SPECULOOS-S	08 Jun 2019	B	484	15	280	5.02	$f(t^1, a^1)$	0.0034	0.63	1.93	1.20
TESS	07/03 – 02/04/2021	TESS	-	600	-	-	-	0.0012	0.94	1.00	0.94
TESS	10/03 – 06/04/2023	TESS	-	120	-	-	-	0.0025	0.97	1.02	0.99

Table 4: The table shows the observational and MCMC analysis parameters. *Observation parameters*: date of observation, telescope, filter(s) used, number of images, exposure time(s), observation duration and FWHM of the point-spread function. *MCMC analysis parameters*: selected baseline-function, standard deviation (RMS) of the best-fitting residuals, deduced values of β_{white} , β_{red} and the coefficient correction $CF = \beta_{\text{white}} \times \beta_{\text{red}}$. For the baseline-function, $f(\varepsilon^n)$, denotes, respectively, the n -order polynomial function of the airmass ($\varepsilon = a$), FWHM ($\varepsilon = f$), background sky ($\varepsilon = b$), x & y positions ($\varepsilon = xy$), and the time ($\varepsilon = t$). The symbol O denotes an offset fixed at the time of the meridian flip.

Parameter	Symbol	Value	Value	Unit
		(Circular, $e = 0$)	(Eccentric, $e \neq 0$)	
<i>Jump parameters</i>				
Planet/star area ratio	$(R_p/R_\star)_{Ic+z}^2$	1.42 ± 0.08	1.41 ± 0.08	%
	$(R_p/R_\star)_{Sloan-z}^2$	1.30 ± 0.09	1.31 ± 0.09	%
	$(R_p/R_\star)_{Johson-B}^2$	1.44 ± 0.18	1.45 ± 0.18	%
	$(R_p/R_\star)_{Blue-Blocking}^2$	1.26 ± 0.17	1.28 ± 0.16	%
	$(R_p/R_\star)_{TESS}^2$	1.24 ± 0.11	1.24 ± 0.11	%
Impact parameter	$b' = a \cos i_p / R_\star$	$0.306_{-0.110}^{+0.077}$	$0.309_{-0.160}^{+0.094}$	R_\star
Transit duration	W	0.1812 ± 0.0018	0.1812 ± 0.0022	days
Transit-timing	T_0	7781.66563 ± 0.00055	7781.66567 ± 0.00056	BJD - 2450000
Orbital period	P	6.2463345 ± 0.0000003	6.2463345 ± 0.0000003	days
RV semi-amplitude	K	14.9 ± 3.1	14.8 ± 3.0	m s^{-1}

Table 5: Jump parameters used in our global MCMC analysis.

JD - 2.450.000	RV [Km/s]	σ_{RV} [Km/s]	Instrument
7189.495005	-3.20480	0.03043	Euler-1.2m/CORALIE
7192.541007	-3.21921	0.07803	Euler-1.2m/CORALIE
7370.835932	-3.21178	0.03220	Euler-1.2m/CORALIE
7399.808035	-3.13149	0.04401	Euler-1.2m/CORALIE
7407.794853	-3.20625	0.02373	Euler-1.2m/CORALIE
7433.698835	-3.18020	0.02095	Euler-1.2m/CORALIE
7748.849031	-3.24191	0.05906	Euler-1.2m/CORALIE
7750.849267	-3.22754	0.03067	Euler-1.2m/CORALIE
7752.804569	-3.18884	0.05035	Euler-1.2m/CORALIE
7917.511102	-3.16284	0.02673	Euler-1.2m/CORALIE
8277.509694	-3.15936	0.03543	Euler-1.2m/CORALIE
8298.463390	-3.16139	0.03678	Euler-1.2m/CORALIE
8520.833792	-3.20823	0.01026	ESO-3.6m/HARPS
8537.867181	-3.17957	0.00695	ESO-3.6m/HARPS
8539.862413	-3.17219	0.00829	ESO-3.6m/HARPS
8540.782640	-3.18160	0.00684	ESO-3.6m/HARPS
8541.860510	-3.16300	0.00551	ESO-3.6m/HARPS
8542.824208	-3.16043	0.00537	ESO-3.6m/HARPS
8543.807974	-3.18210	0.00820	ESO-3.6m/HARPS
8660.500666	-3.14632	0.01434	ESO-3.6m/HARPS
8661.541276	-3.16883	0.01107	ESO-3.6m/HARPS
8670.484865	-3.18669	0.00619	ESO-3.6m/HARPS
8684.509150	-3.16585	0.01232	ESO-3.6m/HARPS

Table 6: Radial-velocities measurements for WASP-193 obtained from Euler-1.2m/CORALIE and ESO-3.6m/HARPS spectrographs.